Optimization of Hypersonic Airbreathing Propulsion Systems through Mixed Analysis Methods

Andrew B. DellaFera

Thesis submitted to the Faculty of the

Virginia Polytechnic Institute and State University

in partial fulfillment of the requirements for the degree of

Master of Science

in

Aerospace Engineering

Jonathan T. Black, Chair

Daniel D. Doyle

Colin S. Adams

K. Todd Lowe

Russell M. Cummings

September 27th, 2019

Blacksburg, Virginia

Keywords: Hypersonic, Propulsion, Optimization

Optimization of Hypersonic Airbreathing Propulsion Systems through Mixed Analysis Methods

Andrew B. DellaFera

(ABSTRACT)

Accurate flow path modeling of scramjet engines is a key step in the development of an airframe integrated engine for hypersonic vehicles. A scramjet system model architecture is proposed and implemented using three different engine components: the isolator, combustor, and nozzle. For each component a set of intensive properties are iterated to match prescribed conditions, namely the mass flow. These low-fidelity one-dimensional models of hypersonic propulsion systems are used in tandem with Sandia Labs' Dakota optimization toolbox with the goal of accelerating the design and prototyping process. Simulations were created for the various components of the propulsion system and tied together to provide information for the entire flow-path of the engine given an inlet state. The isolator model incorporated methods to compute the intensive properties such as temperature and pressure of the flow path whether a shock-train exists internally as a dual-mode ramjet or if the engine is operating as a pure scramjet with a shock free isolator. A Fanno flow-like model was implemented to determine the friction losses in the isolator and a relation is iterated upon to determine the strength and length of the shock train. Two combustor models were created, the first of which uses equilibrium chemistry to estimate the state of the flow throughout the combustor and nozzle. Going one step further, the second model uses a set of canonical reactors to capture the non-equilibrium effects that may exist in the combustor/nozzle. The equilibrium combustor model was created to provide faster calculations in early iterations, and the reactor model was created to provide more realistic data despite its longer computational time. The full engine model was then compared and validated with experimental data from a scramjet combustor rig. The model is then paired with an optimization toolbox to yield a preliminary

engine design for a provided design space, using a finite element analysis to ensure a feasible design. The implemented finite element analysis uses a coarse mesh with simple geometry to reduce computational time while still yielding sufficiently accurate results. The results of the optimization are then available as the starting point for higher fidelity analyses such as 2-D or 3-D computational fluid dynamics.

Optimization of Hypersonic Airbreathing Propulsion Systems through Mixed Analysis Methods

Andrew B. DellaFera

(GENERAL AUDIENCE ABSTRACT)

Ramjets and scramjets are the key to sustained flight at speeds above five times the speed of sound. These propulsion systems pose a challenging simulation environment due to the wide range of flow seen by the system structure. A scramjet simulation model is formulated using a series of combustion models with the goal of accurately modelling the combustion processes throughout the engine. The combustor model is paired with an isolator model and the engine model is compared against previous studies. A structural analysis model is then paired with the engine simulation, and the combined model is used within an optimizer to find an optimum design.

Contents

List of Figures

List of Tables

List of Abbreviations

Acronyms

AFRL Air Force Research Laboratory

AIAA American Institute of Aeronautics and Astronautics

ATACMS Army Tactical Missile System

CFD Computational Fluid Dynamics

CPGS Conventional Prompt Global Strike

CPPFR Constant Pressure Plug-Flow Reactor

CReSS Canonical Reactor Scramjet Simulation

DARPA Defense Advanced Research Projects Agency

DNS Direct Numerical Simulation

DoD Department of Defense

EHTV European Hypersonic Transport Vehicle

FEA Finite Element Analysis

FEM Finite Element Method

GPS Global Positioning System

HCM Hypersonic Cruise Missile

$HPCMP$ High Performance Computing Modernization Program

$HSMW$ High Speed Maneuvering Weapon

$HVFP$ Hypersonic Vehicle Flight Prediction

$HVSI$ Hypersonic Vehicle Simulation Institute

$ICBM$ Intercontinental Ballistic Missile

LES Large Eddy Simulation

$NASA$ National Air and Space Agency

$NASP$ National AeroSpace Plane

$NATO$ North Atlantic Treaty Organization

ODE Ordinary Differential Equation

PFR Plug-Flow Reactor

$RANS$ Reynolds-Averaged Navier Stokes

$RBCC$ Rocket-Based Combined Cycle

$SBLI$ Shock-Boundary Layer Interactions

SRB Solid Rocket Booster

$SSTO$ Single-Stage To Orbit

STS Space Transport System

$TBCC$ Turbine-Based Combined Cycle

$V\&V$ Verification and Validation

$VPFR$ Viscous Plug-Flow Reactor

WSR Well-Stirred Reactor

$WWII$ World War II

Greek Symbols

α Thermal diffusivity

δ Deflection angle

γ Ratio of specific heats

ν Kinematic viscosity

ϕ Equivalence ratio

ρ Density

σ Wave angle

Subscripts

0 Total or stagnation state

a Air/Oxidizer stream

f Fuel stream

i Property of the i^{th} species

n normal component

$prod$ Products

$reac$ Reactants

s Static state

$stoic$ Stoichiometric state

t tangential component

Symbols

Δh_c Heat of combustion

$\dot{m}$ Mass flow rate

τ_0 Wall shear stress

$\boldsymbol{T}$ Thrust

A Area

a Speed of sound, $a = \sqrt{\gamma(R_u/MW)T}$

c Cross-section perimeter

C_f Local Coefficient of friction, $C_f = \tau_0/(\frac{1}{2}\rho {V_o}^2)$

C_p Specific heat at constant pressure

c_t Thrust Specific Fuel Consumption, $c_t = \dot{m}_f/\boldsymbol{T}$

cs Control surface

cv Control volume

D_h Hydraulic diameter

e_0 Energy per unit mass

F Generalized force

g Acceleration of gravity, $g = 9.81\ m/s^2$

h Mass-specific Enthalpy

h_{conv} Heat transfer coefficient

I_{sp} Specific Impulse, $I_{sp} = \boldsymbol{T}/(\dot{m}_f g)$

k Specific heat capacity

L/D Lift-to-Drag Ratio

M Mach number, $M = V_o/a$

m_i Mass of the i^th species in a mixture

MW Molecular Weight

n_i Number of moles of the i^th species in a mixture

Nu Nusselt Number, $Nu = h_{conv}/k$

p Pressure

Pr Prandtl Number, $Pr = \nu/\alpha$

r Recovery factor

R_u Universal gas constant, $R_u = 8.314\ kJ/kmol/K$

Ra Vehicle Range

Re Reynolds number, $Re = \rho V D_h/\nu$

s Mass-specific Entropy

St Stanton Number, $St = h_{conv}/(\rho u_e c_p)$

T	Temperature
t_R	Residence time
T_{ad}	Adiabatic flame temperature
T_{aw}	Adiabatic wall temperature
u	Velocity in the x direction
V	Volume
v	Velocity in the y direction
V_o	Magnitude of velocity vector, $V_o = \sqrt{u^2 + v^2 + w^2}$
w	Velocity in the z direction
X_i	Species Mole Fraction, n_i/n_{tot}
Y_i	Species Mass Fraction, m_i/m_{tot}

Chapter 1

Motivation and Background Information

The design process of aircraft propulsion systems, in general, is a complicated process that requires hundreds to thousands of iterations, the majority of which are completed with low-fidelity simulations. Low-fidelity simulations are typically simulations that trade accuracy of results for decreased computational time do not capture certain phenomena like re-circulation zones. These simulations can be created from physics-based or experimental relationships, and typically simulate 1 or 2 dimensions. Selection and variation of parameters to increase performance characteristics requires significant prior experience and background. Before moving onto the prototyping phase, the design is analyzed through higher resolution simulations to ensure feasibility and decrease the risk of testing. This iterative process, while requiring significant computational time, is one that can be improved through optimization methods in which there is a sufficiently defined design space and detailed analysis tools for refining the design.

Supersonic combustion ramjets, also called scramjets, provide performance gains not seen through other propulsion systems, as well as unique technical challenges. Due to its similarities with the ramjet in operation and modelling, this work uses the two terms interchangeably despite the differentiating factor. On a conceptual level, the ramjet is a

very simple engine with no moving parts, using ram-air compression instead of an active compressor. Due to the lack of compressor and turbine blades, the ramjet can reach speeds far above the limit of turbo-shaft propulsion systems of around Mach 3. Unlike rocket systems, ramjets do not need to carry an on-board oxidizer, decreasing the mass needed to keep the system operational [1].

Ramjets are a unique propulsion system in that they are an efficient system at high speeds; however, they are incapable of producing thrust when stationary due to their use of ram-air compression [1]. Extending this, it has been found that the efficiency of ramjets drops significantly at flight speeds below Mach 2. The inefficiency at low speeds has led to many vehicle designs with either secondary propulsion systems such as rockets or turbojets, or vehicles that are accelerated to operational speeds using an external booster [9]. The lack of stationary thrust has led to the conceptualization and development of the combined cycle engine, in which a dual-mode ramjet shares components with another propulsion system. Such a system can be seen below in Fig. 1.1 which depicts the combined cycle engine used on the European Hypersonic Transport Vehicle (EHTV) that began development in the late 1980's.

1.1 Efforts for Development

This section does not attempt to capture all ramjet implementations but rather details the major design philosophies and describes the development efforts on-going today. It is critical to understand the environment that motivates this research and what it implicates for the future of hypersonic airbreathing flight.

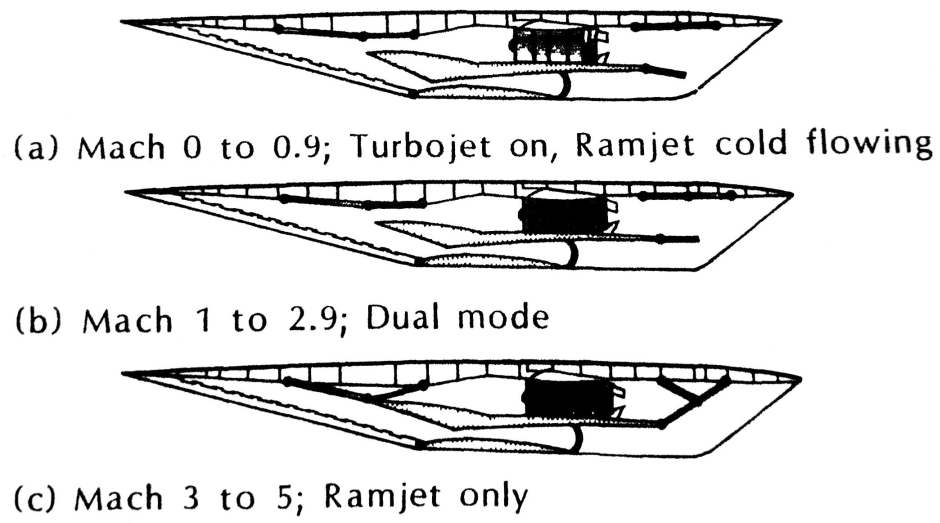

Figure 1.1: Conceptual diagram of the combined cycle engine for the EHTV transitioning from a) pure turbojet flight to c) full ramjet flight [1]

1.1.1 A Brief History of the Ramjet and Scramjet

Although the ramjet and scramjet may seem like new technologies with the increasing numbers of hypersonic vehicles in development, the history of the ramjet began in 1913. A Frenchman, Rene Lorin, is considered to be the first person to theorize ram-air compression in a propulsion system, the key operational concept of ramjets [1]. He did not pursue this concept further at the time as he was focused on low subsonic speeds, the regime in which ramjets are the least effective. Years later, the turbojet was theorized and soon became the propulsion choice for a wide variety of aircraft [9].

While the turbojet revolution was occurring, a few patents were granted for technologies and aircraft relevant to ramjets. The aircraft patented, then known as the Leduc Ramjet Powered Aircraft, made its first flight in 1949. Following the Leduc 0.10 were the Leducs 0.16 and 0.21 reaching speeds of roughly Mach 0.9 [1].

Following the Leduc were the designs of Nord-Aviation in France, who decided to

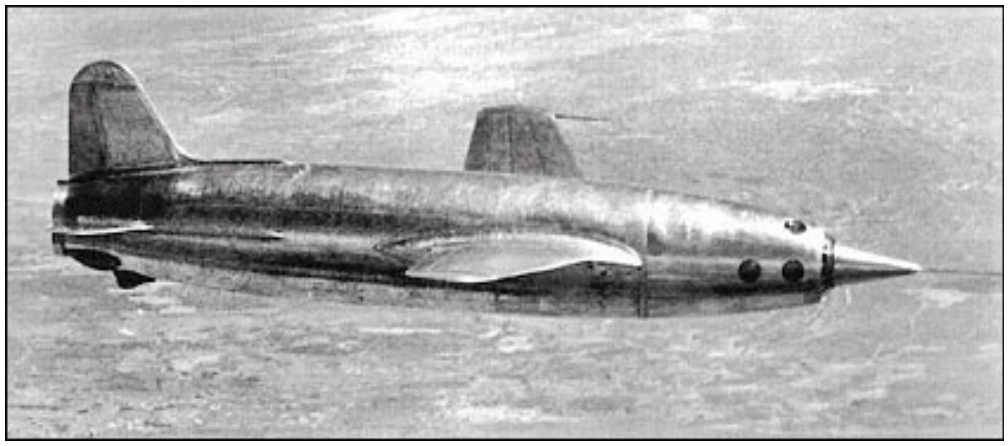

Figure 1.2: The Leduc 0.10 in flight [2]

take advantage of the turbojet technology available at the time. The design produced, named the Griffon II, was powered by a turboramjet, one of the first turbine-based combined cycle engines (TBCC) created. With this new propulsion system, the Griffon II was capable of flying at speeds over Mach 2, and unlike the Leduc designs was capable of taking off on its own [1]. The turboramjet design went on to see various other designs, most notably in the Lockheed Martin SR-71 Blackbird.

In the United States, the majority of the ramjet and scramjet development was performed for military applications. The first "pure" ramjet flight of a manned system took place in 1946 when The Marquardt Aviation Corporation modified a Lockheed F-80 to incorporate ramjets mounted on its wingtips [1]. This flight was followed by a number of ramjet and scramjet powered vehicles with the intent of maturing technology for use in surface-to-air missiles [3]. This effort was motivated in part by the experiences of the United States Navy in the Pacific theater in World War II (WWII), and led to the development of aircraft interceptor missiles in the Bumblebee program which will be discussed in a later section..

Engine/vehicle	Engine type	Dates (year)	Cruise Mach no.	Cruise altitude (ft × 1000)	Powered range (nmi)	Launcher	Total length (in.)	Sustainer length (in.)	Diameter (in.)	Total weight (lbm)	State of development
Ramjets											
Cobra	LFRJ	1945–46	2.0	20	—	Rail	—	—	6	240	Flight demonstration
BTV	LFRJ	1947–48	2.4	30	10	Rail	—	—	18	—	Flight demonstration
RTV	LFRJ	1949–50	2.4	30	25	Rail	—	—	24	—	Flight demonstration
Talos	LFRJ	1950–80	2.7	70	120	Rail	386	254	28	7720	Operational
Triton/SSGM	LFRJ	1951–58	3.0	70	>2000	Rail/sub.	—	—	—	—	Component tests
RARE	SFIRR	1955–60	2.3	—	—	Rail	120	120	5	153	Flight tests
Typhon	LFRJ	1957–65	4.1	100	200	Rail	333	185	16.75	6160	Flight tests
CROW	SFIRR	1956–64	3.0	50	97	Air	127	127	8	370	Flight tests
ATP/TARSAM-ER	ADR	1965–71	3.8	50–70	160	Rail	348	186	13.5	6420	Component tests
ATP/TARSAM-MR	ADR-IRR	1965–71	3.8	50–70	80	Rail	200	200	13.5	1750	Component tests
IRR-SAM	LFIRR	1966–70	3.3	80	—	Rail	220	220	14.75	2200	Component tests
ALVRJ	LFIRR	1968–79	3.0	30	100	Air	179	179	15	1480	Flight tests
IRR-SSM	LFIRR	1971–74	2.5	50	—	Rail	200	200	14.75	2000	Free-jet tests
ASAR	LFIRR	1972–81	3.8	80	—	VLS	220	220	16	2650	Semi-free-jet tests
GORJE	LFIRR	1972–76	2.6	0	35	Air	168	168	12	750	Semi-free-jet tests
MRE	LFIRR	1973–77	3.0	30–70	150	Air	168	168	15	1500	Free-jet tests
IRR-TTV/TTM	LFIRR	1974–85	3.0	60	—	Submarine	246	246	21	3930	Component tests
SOFRAM	SFIRR	1976–81	>3.0	—	150	Air	144	144	8	650	Free-jet tests
LIFRAM	LFIRR	1976–80	>3.0	—	150	Air	144	144	8	650	Semi-free-jet tests
ACIMD	LFIRR	1981–84	—	—	—	Air	144	144	9	—	Component tests
Vandal (Talos)	LFRJ	1983–present	2.2	0	43.5	Rail	434	302	28	8210	Operational
SFIRR	SFIRR	1984–89	2.5	0	50	Air	168	168	18	—	Component tests
SLAT	LFIRR	1986–92	2.5	0	50	Air	216	216	21	—	Flight tests
LDRJ	LFIRR	1995–present	4.0	—	—	Air	—	—	21	—	Planned flight tests
Scramjets											
External burn	ERJ	1957–62	5–7	—	—	—	—	—	—	—	Combustion tests
SCRAM	LFSJ	1962–77	7.5	100	350	Rail	288	158	26.2	5470	Free-jet tests
WADM	DCR	1977–86	4–6	80–100	—	VLS	256	183	21	3750	Component tests
Counterforce	DCR	1995–present	4–6	80–100	—	VLS	256	183	21	3750	Component tests

ACIMD = Advanced Common Interceptor Missile Demonstrator; ADR = air-ducted rocket; ALVRJ = Advanced Low-Volume Ramjet; ASAR = Advanced Surface-to-Air Ramjet; ATP = Augmented Thrust Propulsion; BTV = Burner Test Vehicle; CROW = Creative Research on Weapons; RTV = Ramjet Test Vehicle; DCR = dual combustor ramjet; ER = extended range; ERJ = external ramjet; GORJE = Generic Ordnance Ramjet Engine; IRR = integral rocket ramjet; IRR-SAM = IRR Surface-to-Air Missile; IRR-SSM = IRR Surface-to-Surface Missile; IRR-TTV/TTM = IRR Torpedo Tube Vehicle/Torpedo Tube Missile; LDRJ = Low-Drag Ramjet; LFIRR = liquid-fueled IRR; LIFRAM = liquid-fueled ramjet; LFRJ = liquid-fueled ramjet; MR = medium range; MRE = Modern Ramjet Engine; RARE = Ram Air Rocket Engine; SCRAM = Supersonic Combustion Ramjet Missile; SFIRR = solid-fueled IRR; SLAT = Supersonic Low Altitude Target; SOFRAM = solid-fueled ramjet; SSGM = Surface-to-Surface Guided Missile; TARSAM = Thrust Augmented Rocket Surface-to-Air Missile; WADM = Wide-Area Defense Missile.

Figure 1.3: U.S. Navy ramjet evolution [3]

As Fig. 1.3 shows, there have been a myriad of different ramjet programs over the years from the U.S. Navy alone, many of which never reached flight testing or operational maturation. It should also be noted that scramjet development had not been the focus of development until the 1950s when it was found that ramjets lost efficiency at flight speeds exceeding Mach 6 due to the deceleration of intake air to subsonic speeds [1]. This caused the focus to shift to supersonic combustion as the way to reach even higher speeds.

1.1.2 Existing Studies and Experiments

Outside of direct defense applications, other hypersonic programs existed to either use scramjet technology or to further its maturation. Described here are the most notable and most relevant programs.

National AeroSpace Plane

One of the more notable was the NASP program that aimed to produce a single-stage-to-orbit (SSTO) vehicle with horizontal launch and landing capabilities. Such a vehicle was seen as the replacement for the Space Shuttle and envisioned to provide lower launch costs due to reusability and greater availability resulting from its horizontal launch capability [16]. Created in 1986, the NASP program performed various studies crucial to both hypersonic flight and scramjet development through various risk reduction projects and ground tests. Despite its technological contributions and DoD support, the NASP program suffered restructuring activities and budgetary issues which led to the program's official termination in 1995 [16].

Hyper-X Program and the X-43 Flight Vehicle

All of these programs, successes and failures, have led to the modern day airframe integrated scramjet, the first of its kind being flown on the X-43 vehicle from the Hyper-X program [17]. The Hyper-X program showed that scramjets are feasible for powered flight while at the same time highlighting some crucial issues that might arise, such as a lack of readily-available launch vehicles capable of accelerating the vehicle to operational speeds at or above Mach 4. Following a launch vehicle failure on the first flight, the second and third flights reached Mach numbers of 7 and 9.68 respectively, answering the question of "will scramjets work in flight" [17].

X-51 Waverider

Following the success of the Hyper-X program was an AFRL program, given the X-51 designation, that had the goal of proving scramjets were capable of sustaining extended flight. The X-51A vehicle, seen in Fig. 1.4, took on geometry akin to a hypersonic cruise missile (HCM) and used more practical fuel than the liquid hydrogen its predecessors used [18]. Similar to the X-43, it was an air-launched vehicle with a booster stage, however, the booster stage here was a modified Army solid rocket booster (SRB) used by the Army Tactical Missile System (ATACMS) instead of a modified Pegasus launch vehicle [4].

After numerous design iterations, ground tests and risk reduction procedures, the X-51A flight vehicle conducted 210 seconds of scramjet powered flight, confirming the predicted long range capabilities of scramjets [19]. Additionally the X-51A flight showed the benefits of regenerative cooling with endothermic hydrocarbon fuels for hypersonic flight, a key operational concept for extended scramjet flight [20]. The X-51A program ended in 2013

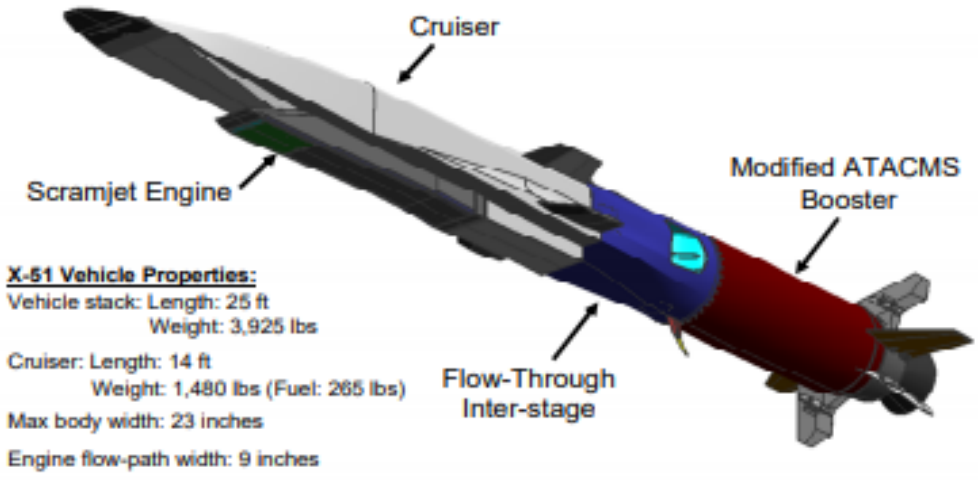

Figure 1.4: The X-51A Scramjet Engine Demonstrator-WaveRider Vehicle [4]

and provided critical information for on-going and future scramjet propelled programs.

1.1.3 Hypersonic Vehicle Simulation Institute (HVSI)

With the previously described programs and modern computational resources, one might think that the predictive capabilities of computational tools would be sufficient to support new programs. While it is true that current capabilities are better than in the past, the DoD's High Performance Computing Modernization Program (HPCMP) and USAF have decided that there are critical science phenomena that modern computational codes lack. According to Cummings and Morton, hypersonic flight, in general, has suffered from both cyclical funding and a lack of knowledge, both of which have led to program cancellations and critical mission failures [21]. The effects of cyclical funding can be seen throughout history and are not unique to the field of hypersonics. Many programs, such as the Constellation[22] manned flight or NASP [16] programs, have been cancelled due to funding cycles or political shifts. Although with each program cancellation some "lessons learned" are recorded and held on to for the next program, much information is lost whether it be test data or general

expertise in the area.

The Hypersonic Vehicle Simulation Institute (HVSI) has recently been created with various objectives relevant to hypersonic computational capabilities, the first being to "facilitate the development and documentation of" hypersonic vehicle simulation by unifying the various government agencies, industry, and academic organizations involved in the development of hypersonics [21]. In other words, the HVSI is meant to pull together the various resources and knowledge bases to reach a common goal. The second objective is to assist in the funding research projects that benefit hypersonic simulation capabilities of the DoD. This objective pairs with the next, which is to help bring hypersonic research into "production quality simulation software available to government, academic, and industry acquisition partners" [21]. The last two objectives are to create a repository of hypersonic V&V data, and to provide computational resources to programs in order to accelerate the hypersonic vehicle development and acquisition.

With the HVSI purpose described, it is important to explain why it is relevant to the work described later. While much of the focus of HVSI is initially on developing hypersonic turbulence models, it is also focused on research in Shock-Boundary-Layer Interactions (SBLI), fluid/thermal/structural interactions, and non-equilibrium chemistry modeling [21]. These three areas, in addition to turbulence models, are critical to the development and modeling of scramjet engines as well as other vehicles and propulsion systems.

1.2 Uses of Scramjets

With the focus of this paper on the design and analysis of a scramjet, it is necessary to describe what applications they may be used for and what kind of environments the system

may see. The future applications also give some background as to why this is still a research focus for many government organizations, academic institutions, and industry experts.

1.2.1 Orbital Launch

As a result of the advancement of technology, the access to space is seen as a necessity for countries as more technologies (i.e. communications, GPS, etc) and capabilities become dependent on connections to satellites. This is not news, however, it is unlikely that countries will ever depend less on satellite services resulting in increasing importance on launch capabilities. As scramjets were developed and tested, it was considered that such propulsion systems might grant immense benefits to launch vehicles in both payload mass to orbit and cost-efficiency. This results in the importance of the airbreathing element of scramjets. Instead of carrying oxidizer throughout the flight like rockets, the engine uses the atmosphere as the oxidizer [18]. This can also be seen in Fig. 1.5, where it is seen that scramjets have a significantly higher specific impulse, the impulse produced per unit mass of expended propellant, than rockets up to roughly Mach 12. In this paper as well as relevant literature, the specific impulse is used as a performance variable measuring the impulse per unit mass of fuel [9].

Although scramjets are more efficient, they do face the issue of not being able to intake enough air for combustion at very high altitudes. Due to this operational shortfall, a scramjet powered orbital launch vehicle would need some sort of rocket propulsion to complete its flight to orbit. Similar to the combined cycle engine used on the Nord-Aviation Griffon II, researchers are looking into a rocket-based combined cycle (RBCC) engine, which would have a scramjet and rocket engine sharing hardware [9, 23]. Such a development could revolutionize space launch and be the key to developing a SSTO vehicle similar to NASP,

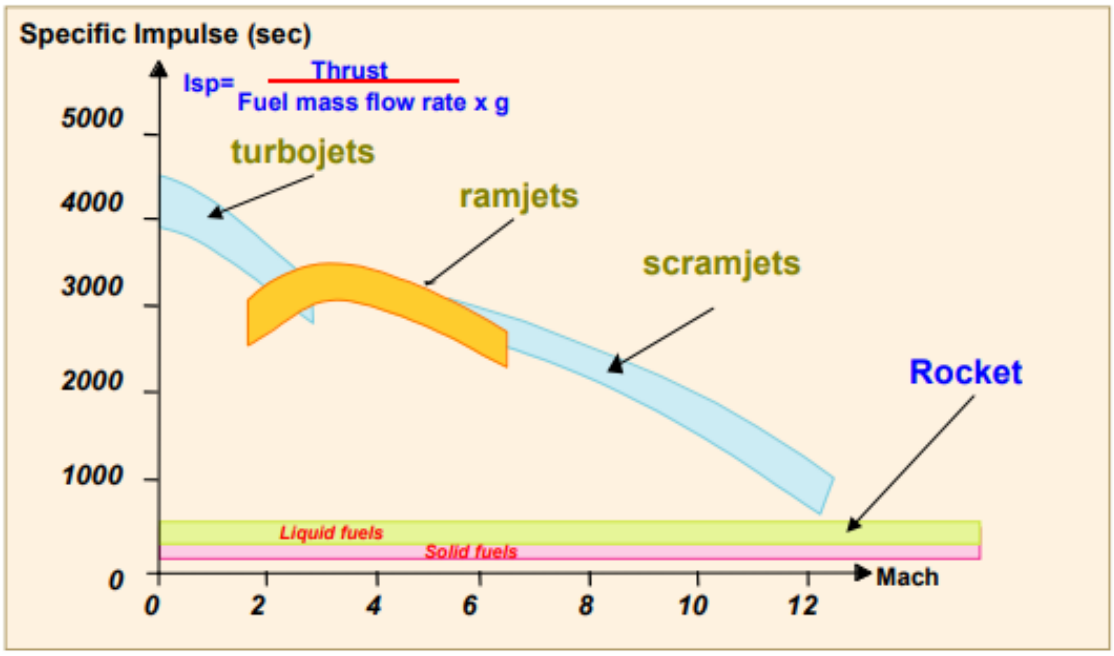

Figure 1.5: Achievable performance of various propulsion types [5]

however, it is dependent on the maturation of scramjets.

1.2.2 Global Strike

Much of the early development of scramjets was performed with the intention of increasing range and payload capacity for a variety of missiles, and while there are other applications, long range missiles are still the most common. It is of interest to the defense community to have the capability to reach specified targets anywhere on the planet within an hour, however, the funding for such projects has been restricted in the past [24]. For an intercontinental ballistic missile (ICBM), these targets would have to be stationary, but with the maneuverability of a hypersonic cruise missile, that target envelope is expanded to "slowly" moving targets [18]. With the recent announcements from foreign adversaries [18], the funding for conventional prompt global strike (CPGS) weapons has been increased and

is projected to continue increasing for at least the next 5 years [24]. It should be noted that the maturation and developments from individual programs like these initiatives and HVSI will mutually benefit each other.

1.2.3 Defensive Interceptor

Following the recent increase of publicly known global strike weapons, specifically high speed maneuvering weapons, many programs were conceived to counter such vehicles. These defensive measures, known as hypersonic interceptors, have existed at least conceptually since 1944. The defensive interceptor concept was born when the U.S. Navy was looking for a way to defend large ships from aircraft, a problem faced in the Pacific theater of WWII [3, 25].

Having the capability to neutralize threats to the fleet at medium to long range was a high priority to the U.S. Navy, and scramjets were the key to developing such vehicles. This anti-aircraft missile program was designated Operation Bumblebee, and led to the development of various surface-to-air high speed missiles [25], many of which can be found listed in Fig. 1.3. Over time, the surface-to-air focus shifted from anti-aircraft to anti-missile, which can be seen by both the functionality of both the Patriot and THAAD programs, however, they are more focused on ballistic missile defense [26].

While the development of these systems has never stopped, the announcements of operational high-speed maneuvering weapons (HSMWs) by Russia and China has re-ignited the motivation for the development of both global strike weapons and anti-missile systems, specifically counter-HSMWs [18]. The capabilities of HSMWs make them nearly untouchable to conventional defenses due to their high altitude, high speed, and high maneuverability.

The capability to maneuver is the major distinction from ICBMs, as HSMWs can change their trajectory mid-flight, whereas ICBMs have a predictable "ballistic" trajectory. In response there has been a surge in funding for missile defense capability in development of hypersonic interceptor vehicles that would mend the perceived gap in defensive capabilities [27].

1.3 State of Computational Models, Verification and Validation

Simulation of ramjets are a critical portion of both hypersonic vehicle development and propulsion system development. To provide accurate results and assist in the testing of such propulsion systems, it is important to understand the current state of high speed computational models. In 2017, a Hypersonic Vehicle Flight Prediction (HVFP) workshop was held to discuss the capabilities and pitfalls of modern hypersonic computational codes [21]. This HVFP workshop decided that the current models lack a number of crucial scientific aspects; the most relevant to this study being high speed combustion physics, non-equilibrium chemistry, and fluid-thermal-structural interaction. It was also emphasized that there are no well defined turbulence models created specifically for high speed flows, which casts a significant amount of uncertainty on all related computational fluid dynamics (CFD) results.

The shortcomings of current models stems from the lack of available test data relevant to hypersonic vehicles. Tests of these vehicles are expensive and time consuming, and as shown by the Hyper-X program the costs of flight tests can grow due to unanticipated technical challenges [17]. Flight tests are crucial as ground tests have been found to leave many unknowns about full vehicle designs as the facilities to perform full scale tests are prohibitively expensive [5]. The two kinds of ground tests that can be done with scramjets

are free-jet tests and direct-connect tests. Free-jet tests involve a larger wind tunnel with a full engine including the inlet and cowl, while the direct-connect tests are purely a facility nozzle feeding directly into a scramjet combustor upstream of the nozzle/diffuser [28]. Direct-connect tests are much more common and less expensive than free-jet tests, however, direct-connect tests do not accurately simulate the conditions seen by the combustor as the facility nozzle typically creates a uniform flow. There have been attempts to use distortion generators to mimic the flight conditions downstream of the inlet [28, 29], but there is still more exploration to be done in this area.

Multiple open-source CFD solvers such as HyFOAM and Eilmer have been created specifically for hypersonic flows and supersonic combustion [30], however, like proprietary software they suffer from the lack of supersonic and hypersonic turbulence models [21]. This issue can be eliminated with experiments designed to measure turbulence followed by a comprehensive effort to create correlation between the various gas properties and velocities. Open-source CFD solvers have been looked at for use in design optimization studies but the computational time and resources are limiting factors [30].

Outside of CFD, there are numerous models of both empirical derivation and physics based formulation, many of which are 1D models similar to the one developed here. Other models include performance models that do not provide information on the entire flowpath. Both of these are beneficial in conceptual design as the computational time is significantly less than CFD, however they are typically less accurate. This paper proposes a combination of one-dimensional analyses and 3D CFD for proper propulsion system optimization to mitigate the computational time of CFD solvers.

1.4 Objectives and Work Summary

The work described here considers a set of analyses and goals that are common in the development of high-speed propulsion systems. Considering the state of computational models, this work aims to pursue the following objectives:

1. Develop a 1-dimensional scramjet simulation using finite-rate combustion chemistry models

2. Validate the created scramjet simulation using available data

3. Construct an auto-generating structural analysis tool to explore the thermal-structural interactions present in components of scramjet systems

4. Optimize a conceptual engine design for a sample case using the coupled analyses

Pursuit of the first objective led to the development of the Canonical Reactor Scramjet Simulation (CReSS) which was formulated using a combination of empirical and physics-based models. The second objective was fulfilled through comparison with the results of a well-validated computational fluid dynamics model for a specific engine geometry.

The isolator duct was modeled through integration of conservation equations upstream and downstream of a shock train. Determining the shock train length was done using an empirical correlation while the pressure profile was determined using a physics-based pseudo-shock model. CReSS determines the isolator pressure ratio using a set of assumptions to model the isolator-burner interactions. A set of plug flow reactors were created for combustion modeling and a series of assumptions were made to simulate cavity-based flameholders. The developed reactor models were found to simulate both supersonic and

subsonic flow within acceptable accuracy, however, it was found that the current formulation of CReSS has discontinuities in total enthalpy if the flow chokes. This discrepancy causes greater pressure and higher Mach numbers downstream of the choke point but stays within acceptable bounds for low-fidelity modeling.

The structural model was developed using open-source software and autonomously creates a 3D model, a corresponding FEM mesh, and runs a FEA with applied loads imported from CReSS. These linked simulations were then coupled with the Dakota optimization toolbox creating the system shown in Fig. 1.6. This system fulfills the fourth objective

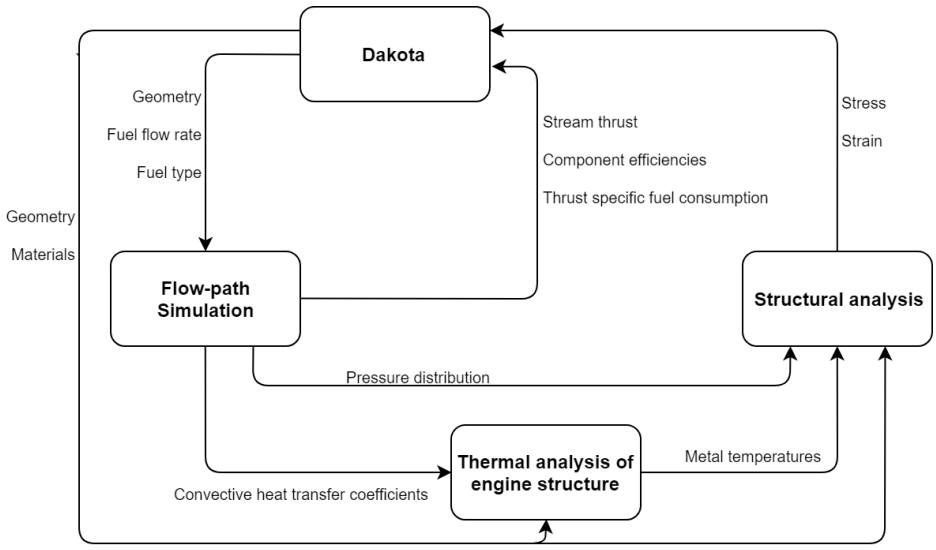

Figure 1.6: Block diagram of the interactions between analyses and optimization toolbox.

and produces a conceptual engine design that is ready to be further developed with higher fidelity simulations.

Chapter 2

Hypersonic Airbreathing Propulsion Primer

A general understanding of high speed flows is necessary to make sense of the work described in later sections, therefore, this chapter will be used to summarize the relevant topics. The first topic discussed is general compressible flow principles and related flow phenomena including shock waves as well as the differences of supersonic and subsonic flow. While subsonic flow is mostly irrelevant to hypersonic vehicles, it is possible to see it within the propulsion system under certain conditions later discussed. Following the general compressible flow discussion is a description of various combustion principles and common simulation methods used for similar systems. This chapter is then completed with a discussion of concepts critical to the operation of hypersonic airbreathing propulsion systems, and a brief description of how each is addressed in this work.

2.1 Compressible Flow Summary

Non-intuitive phenomena exist in compressible flow regimes and are described here with some discussion of the relevance to the later analysis. The phenomena of interest exists in high subsonic to supersonic regimes and covers most of the fluid behavior seen in scramjet

components. How these fluid behaviors are captured by the analysis described is detailed later in 3 of this paper.

2.1.1 Supersonic and Subsonic Principles

It is important to characterize the flows of the different regimes and provide the distinct differences of fluid dynamics as the methods of simulation vary greatly. The separation of the two regimes is centered on the definition of the speed of sound,

$$a = \sqrt{\gamma \frac{R_u}{MW} T_s} \tag{2.1}$$

which, as it's name suggests, defines the speed at which sound travels through a gas of specific heat ratio γ molecular weight MW, and temperature T_s. Using the speed of sound, the Mach number is defined

$$M = \frac{V_o}{a} \tag{2.2}$$

and can be used for determining various flow properties [8, 9, 31]. From the Mach number, the flow can be labeled as subsonic (M $<$ 1), sonic (M $=$ 1), supersonic (1 $<$ M $<$ 5), and lastly hypersonic (M $>$ 5). For most airbreathing propulsion systems, only the subsonic regime is relevant aside from the supersonic inlets seen on high performance aircraft. In ramjets and scramjets, internal flows can range from high supersonic to high subsonic, thus it is necessary to review the dynamics of both regimes.

The subsonic regime is the most familiar, as it is seen in daily fluid flows like the water coming out of a faucet or wind blowing between buildings. Properties of subsonic flow include smooth streamlines free of discontinuities, and flow disturbances propagate upstream and downstream [32]. These characteristics are not all shared with supersonic flows, as

the speed at which information travels in a fluid is the speed of sound [8]. In supersonic flows, disturbances do not propagate upstream and it is possible to see discontinuities in the streamlines caused by shock waves which will be discussed later [8, 32].

For a given control volume, fluid dynamics equations fall into three categories: conservation of mass, momentum, and energy. The general forms of the conservation equations are, in that order,

$$\frac{d}{dt}\int_{cv}\rho dV + \int_{cs}\rho(\mathbf{u}\cdot\mathbf{n})dA = 0 \tag{2.3}$$

$$\frac{d}{dt}\int_{cv}\rho\mathbf{u}dV + \int_{cs}\mathbf{u}\rho(\mathbf{u}\cdot\mathbf{n})dA = \sum F \tag{2.4}$$

$$\frac{d}{dt}\int_{cv}e_0\rho dV + \int_{cs}e_0\rho(\mathbf{u}\cdot\mathbf{n})dA = \int_{cs}\dot{Q}dA - \dot{W}_{shaft} + \int_{cv}\mathbf{X}\cdot\mathbf{u}dV - \int_{cs}p(\mathbf{u}\cdot\mathbf{n})dA \tag{2.5}$$

where $\dot{Q}$ and $\dot{W}_{shaft}$ represent the local heat transfer into the volume and the rate of work done by the control volume [9]. These equations are powerful tools and are extremely useful for a variety of simulations, and will be reduced to simpler forms for the analysis described in later sections.

Thermodynamic processes of systems, and thus fluid dynamics processes, are categorized as ideal or real. Commonly referred to isentropic processes, ideal processes do not have any losses or entropy gain. While it is physically impossible for ideal systems to exist, it is a good approximation for many flows such as non-reacting nozzles or ducts. With some assumptions about the flow, a set of relations exist to relate intensive properties to a reference, or stagnation state. For fluids, the stagnation state is described as the state of the flow if it was brought to rest without any losses. One of the more powerful relations from this definition is that of Stagnation Enthalpy

$$h_0 = h_s + \frac{V^2}{2} \tag{2.6}$$

which clearly provides a relation between the properties of the gas and the kinetic energy [1]. As previously mentioned, there are some assumptions that are involved with using Eq. 2.6, most prominently that the flow is adiabatic($h_0 = constant$). Adiabatic flow is defined as a process that does not involve heat transfer in or out of a system [9], which is a very good approximation for most flow devices such as a nozzle or duct. Additionally, if the flow is assumed to be thermally perfect, the stagnation temperature can be defined as

$$T_0 = T_s(1 + \frac{\gamma - 1}{2}M^2) \tag{2.7}$$

There is also a stagnation pressure, which is considered to be constant if and only if the flow is isentropic. In mathematical terms, isentropic flow can be defined as

$$\frac{p_s}{p_0} = (\frac{T_s}{T_0})^{\frac{\gamma}{\gamma-1}} \tag{2.8}$$

which if combined wit Eq. 2.7 can be manipulated to yield

$$p_0 = p_s(1 + \frac{\gamma - 1}{2}M^2)^{\frac{\gamma}{\gamma-1}} \tag{2.9}$$

where p_0 is the stagnation pressure. The stagnation pressure is constant for isentropic systems, however, many systems and models in this work are assumed to be adiabatic, not isentropic. For a process to be declared isentropic, it must be both adiabatic and reversible, where a reversible process generates no entropy [8]. To determine the entropy change between states 1 and 2, the equation

$$s_2 - s_1 = c_p \ln(\frac{T_2}{T_1}) - R \ln(\frac{p_2}{p_1}) \geq 0 \tag{2.10}$$

can be used where c_p and R are the specific heat at constant pressure and the gas constant, respectively [31]. Before moving on, it is important to note that Eq.2.10 assumes that the specific heats are constant between the two states, or that the gas is calorically perfect [8, 31].

2.1.2 Shock Waves

A high speed flow phenomena of relevancy to this work is that of shock waves and, more relevant to this work, shock wave trains. Shock waves are the means by which an upstream supersonic flow is not affected by downstream disturbances [6, 8]. To help understand shock wave theory, an appropriate metaphor would be a series of blind-folded skiers are going down a hill along the same path, unable to see what is ahead. The first skier runs into a tree, and all of the following skiers proceed to run into the skier ahead of them.

Figure 2.1: Metaphorical shock propagating through a flow suddenly brought to rest [6]

Visualized in Fig. 2.1, the line of skiers represents a streamline of a supersonic flow as it approaches a shock wave, however, instead of being brought to rest, the flow

is decelerated and compressed as the gas particles collide. As a result of the collisions the pressure, temperature, density, and entropy suddenly increase [9]. Shock waves can be visualized using Schlieren imagery as shown in Fig. 2.2, which captures the shock waves produced by a supersonic jet by visualizing the resulting density gradients typically through use of a light source, a set of lenses, and a knife edge or filter [33].

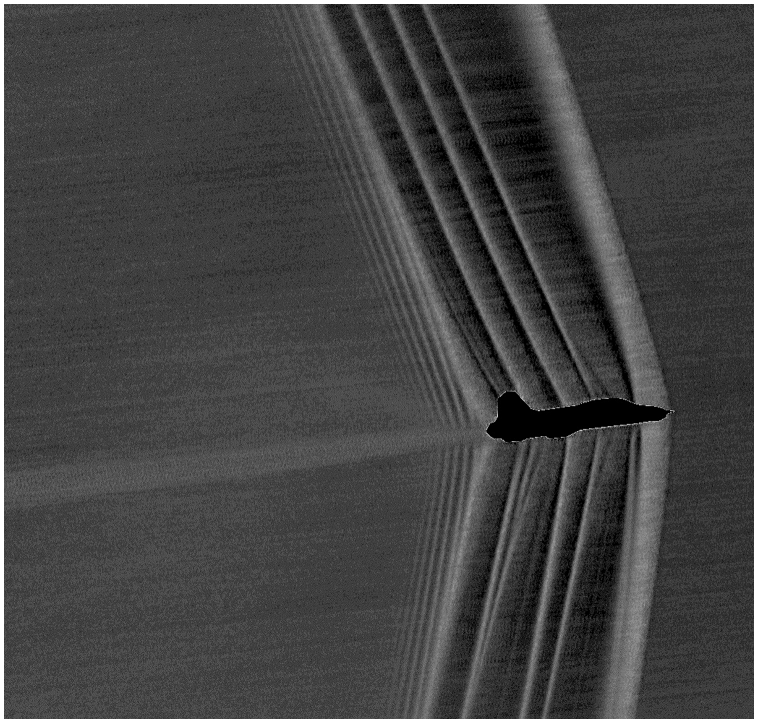

Figure 2.2: Schlieren image of a T-38C in supersonic flight, [7]

In addition to a change in properties, the flow's direction may experience a sudden change in direction depending on the type of shock wave. Two shock waves categories are relevant to this work; normal and oblique shocks. Normal shocks are when the shock forms perpendicular, or normal, to the direction of the flow and thus does not change the flow's direction.

The control volume shown in Fig. 2.3 is the basis of how normal shocks are ana-

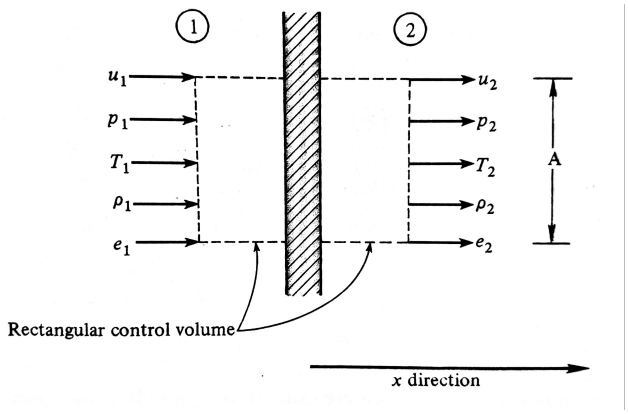

Figure 2.3: Control volume placed around a normal shock [8]

lyzed as the conservation equations described in the previous section are still valid here [9]. Applying Eqs. 2.3, 2.4, and 2.5 to the control volume above yields the quasi one-dimensional equations

$$\rho_1 u_1 = \rho_2 u_2 \tag{2.11}$$

$$p_{s1} - p_{s2} = \rho_1 u_1 (u_2 - u_1) \tag{2.12}$$

$$T_{0,1} = T_{0,2} \tag{2.13}$$

from which many more relations can be derived [9], however, these are sufficient for this section's purpose of introducing shock wave theory. These equations also are then used to derive the general equations for oblique shock waves, which are shock waves not perpendicular to the flow. These waves can be analyzed by applying the normal shock equations to the normal components of the flow as shown below.

As Fig. 2.4 shows, oblique shock waves turn the flow by an angle δ, which results in a shock wave at an angle σ to the upstream flow, and both of these angles are used to determine the downstream properties. The deflection angle δ is normally known as it corresponds to the geometry of the system, which allows for the shock wave angle σ to be determined with the rest of the downstream flow. Applying the normal shock equations to

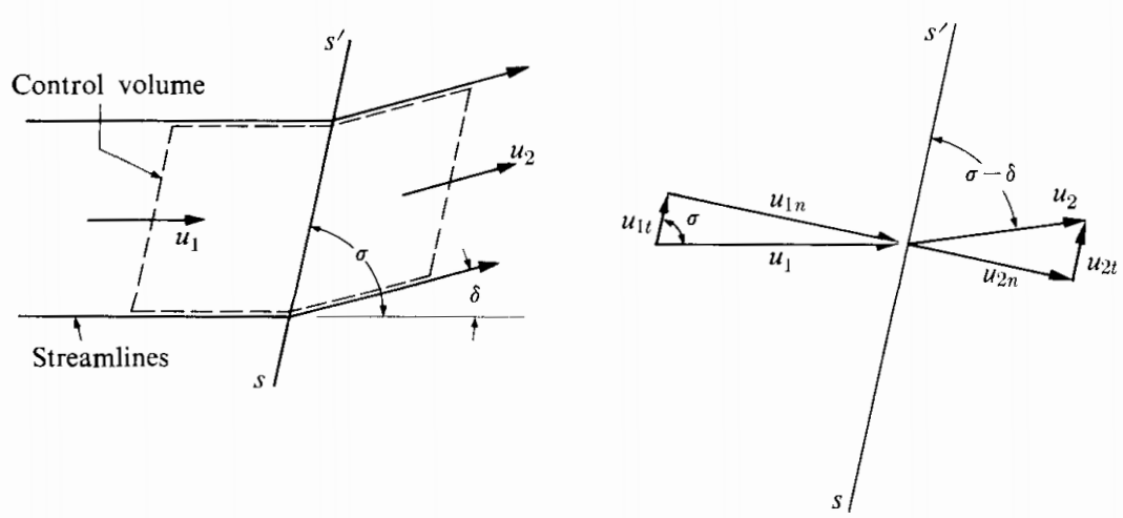

Figure 2.4: Control volume for oblique shock theory [9]

the control volume of an oblique shock wave yields the equations

$$\rho_1 u_{1n} = \rho_2 u_{2n} \tag{2.14}$$

$$p_{s1} - p_{s2} = \rho_2 u_{2n}^2 - \rho_1 u_{1n}^2 \tag{2.15}$$

$$0 = \rho_1 u_{1n}(u_{2t} - u_{1t}) \tag{2.16}$$

$$T_{0,1} = T_{0,2} \tag{2.17}$$

where Eqs. 2.15 and 2.16 are the normal and tangent components relative to the shock wave [6, 9].

To further simplify the analysis, Eq. 2.16 can be reduced to $u_{2t} = u_{1t}$ showing mathematically that the velocity component tangent to the shock wave is constant [6, 8, 9, 31, 32]. Further manipulation of the oblique shock control volume results in a set of equations describing various relations across shock waves in terms of the upstream Mach

number M_1 and the ratio of specific heats γ. For oblique shock waves, the equation

$$\tan(\sigma - \delta) = \frac{2(1 + \frac{\gamma-1}{2} M_1^2 \sin^2 \sigma)}{(\gamma + 1) M_1^2 \sin \sigma \cos \sigma} \tag{2.18}$$

is of importance as it mathematically defines the $\sigma - \delta$ relationship [9] which can then be used to help design aircraft geometry of interest such as high speed inlets. Shown below is one of many contour plots that may be used to visualize Eq. 2.18.

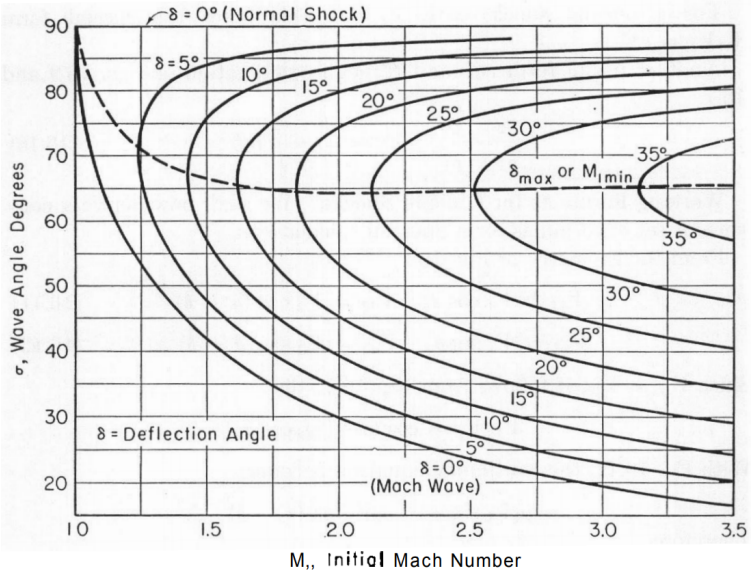

Figure 2.5: Shock angle σ as a function of upstream Mach number with δ contours [6]

This concludes the discussion of general shock wave theory and analysis, however, it should be noted that the description of shock waves is on a macro-scale and for steady state one-dimensional flows. Shock wave structure is much more complex on a micro-scale and more parameters exist when considering three dimensions or transient flows, thus different analysis methods are necessary.

While the presence of shock waves is more noticeable on the external surfaces of hypersonic vehicles, there are a series of shock waves which typically exist inside high speed

propulsion systems. These waves form a "shock train" and act as a compression mechanism upstream of the combustor and adjust the flow to the conditions entering the burner. The internal shock train is typically caused by a back pressure from combustion or the method of fuel injection. Due to the importance of shock waves to the operation of ramjets, shock waves must be considered and simulated.

2.1.3 Non-Isentropic Flows

The flows previously discussed did not explicitly discuss the effects of friction or heat transfer into a flow, and thus those topics will be discussed here. Applying the second law of thermodynamics to a control mass yields

$$ds \geq \frac{\delta q}{T} \tag{2.19}$$

showing the change in entropy must be greater than or equal to the heat transfer rate. Expanding this for adiabatic flows where the heat transfer rate δq is zero, $ds \geq 0$. Thus for systems with heat transfer or friction, an entropy change occurs.

As an improvement over the many inviscid models, Fanno flow refers specifically to the flow of an adiabatic gas through a tube with the inclusion of friction effects in the momentum balance [9, 34]. While it is an improvement, it should be noted that Fanno flow models assume a friction coefficient model which are typically empirically determined and thus have uncertainties. Not including body forces, the integral equations in Sec. 2.1.1 can be written differential form as

$$\frac{dp}{p} - \frac{dT}{T} + \frac{1}{2}\frac{du^2}{u^2} = 0 \tag{2.20}$$

$$\frac{dp}{p} = -\frac{\gamma M^2}{2}(4\frac{C_f dx}{D}) - \frac{udu}{RT} \tag{2.21}$$

$$0 = \frac{dT}{T} + \frac{\gamma - 1}{\gamma}\frac{udu}{RT} \tag{2.22}$$

for a differential element of length dx in the axial direction. The uncertainty mentioned previously comes into this system of equations in the local skin friction coefficient C_f, as it is generally defined as

$$C_f = f(Re, \frac{\mathrm{R}}{D}) \tag{2.23}$$

where Re is the Reynolds number $\rho u D/\mu$, R is the average height of surface roughness elements and D is the duct diameter [9]. The function f can be selected from a variety of options such as the *Thwaites-Walz Method* and the *Blasius Solution*, however, each method is only valid for certain flow conditions, thus it is up to the designer to select the appropriate model [35].

The effects of friction on the flow are somewhat counter-intuitive, as it seems logical that friction would decelerate the flow. For subsonic flow, the fluid accelerates due to friction until it reaches a Mach number of 1. In supersonic flow the fluid is decelerated towards a Mach of 1 resulting in a point referred to as the "critical point" where the Mach is unity. The critical point can then be used to calculate a variety of properties at different locations in the duct [8, 9], however, these relations are outside the scope of this work.

A different non-isentropic flow model is Rayleigh flow, which describes inviscid flow through a constant area duct with a non-zero heat addition rate. Heat addition to a flow could result from processes such as combustion, evaporation/condensation of doplets in the flow, and wall heat transfer [9]. Modelling the heat addition as a change in stagnation

enthalpy dh_0, the conservation equations become

$$\frac{d\rho}{\rho} + \frac{du}{u} = 0 \tag{2.24}$$

$$dp = -\rho u du \tag{2.25}$$

$$dh_0 = dh + udu \tag{2.26}$$

over a differential element in a duct [9].

Similar to Fanno flow, heat addition pushes the flow towards sonic velocity regardless of its current Mach number [6, 8, 9]. This means that subsonic combustors accelerate the flow and supersonic combustors decelerate the flow. The combustor models discussed later do not use Rayleigh flow, however, this summary does provide some background to the flow behavior resulting from the employed models. Additionally, it is possible to use both Fanno and Rayleigh flow models with a varying area, which will be explained and utilized in a later section.

2.2 Combustion Summary

This section describes the topics relevant to the chemical changes and extreme temperature environment which occurs in the combustor of ramjet systems. Correct simulation of combustion processes is not an easy task and would be extremely difficult without access to the computational resources now available. Combustion can be described as the coupling of chemistry kinetics, thermodynamics, and fluid mechanics and thus requires knowledge from each field [10].

Due to the heavy dependence of high speed flows on the enthalpy and chemical composition, accurate combustion models are needed. For lower speed flows, the combustion reaction occurs on timescales orders of magnitude smaller than the fluid dynamics, however, in the high speed flows present in ramjets and scramjets, the timescales are similar, necessitating chemical kinetics modelling [1].

2.2.1 Thermodynamics of Combustion

For this work, the objective of combustion is to obtain the enthalpy change and thermodynamic properties of the flow after fuel addition in order to accurately predict the engine performance. Obtaining these can be done simultaneously through thermodynamic analysis mathematically described as

$$\Delta h_c = h_{reac} - h_{prod} \tag{2.27}$$

where Δh_c is the enthalpy of combustion. As Eq. 2.27 shows, the enthalpy of combustion is equal to the difference in enthalpies of formation between the reactants and products, describing the energy released from chemical reactions [1, 10]. While this equation is useful for understanding combustion, a more practical form is

$$h_{reac}(T_i, P) = h_{prod}(T_{ad}, P) \tag{2.28}$$

which defines a constant-pressure adiabatic flame temperature T_{ad} [10]. The adiabatic flame temperature is the resulting temperature after combustion assuming no heat transfer outside of the system [1, 9, 10] and is a good prediction of the resulting flow. Eq. 2.28 can also be

represented in the form

$$\sum_{react} N_i \overline{h}_i = \sum_{prod} N_i \overline{h}_i \tag{2.29}$$

where N_i is the number of moles per species and $\overline{h}_i$ is the specific enthalpy of species i. This seems to be a simple analysis in theory however, without computational resources it is a tedious process as the temperature of the products, T_{ad} must be iterated to calculate h_i until the system closes [10].

For reference, general hydrocarbon fuel and air combustion can be represented by the reaction

$$C_x H_y + a(O_2 + 3.76N_2) \rightarrow bCO_2 + cCO + dH_2O + eH_2 + fO_2 + 3.76N_2 \tag{2.30}$$

where $a = (x + y/4)/\phi$ and ϕ is the equivalence ratio. Equivalence ratio is a ratio of how much fuel there is compared to the value at which all fuel and oxidizer is consumed by the reaction [10] and will be referred to multiple times throughout this paper.

It should be noted however, that if T_{ad} is found using a stoichiometric analysis such as Eq. 2.30, the calculated temperature will be extremely high. These temperatures are much higher than experimental data, as they do not account for the dissociation of products at high temperatures, which can be captured through equilibrium chemistry modelling [1, 9, 10] discussed in the next section.

2.2.2 Equilibrium Chemistry

One of the most prevalent combustion models used in modeling propulsion systems are based on equilibrium chemistry models. Extending from simple stoichiometric

calculations, chemical equilibrium accounts for dissociation of various compounds at higher temperatures. This dissociation takes energy, and thus will yield lower flame temperatures than those of stoichiometric analyses [10].

Equilibrium models are those that assume that the air-fuel mixture is at the state with the least internal energy, or *Gibbs free energy* as defined by

$$G \equiv H - TS \tag{2.31}$$

using extensive properties. Applying the second law to Eq. 2.31 yields

$$(dG)_{T,P,m} \leq 0 \tag{2.32}$$

stating that the Gibbs function will always decrease for a fixed mass system undergoing a isothermal and isobaric change when the only work is boundary work [10].

Using the defined equilibrium state at which Gibbs free energy is minimum, it is shown that at equilibrium

$$(dG)_{T,P,m} = 0 \tag{2.33}$$

for a given temperature and pressure [1, 10]. Through more manipulation and expansion to mixtures of ideal gases, the equations

$$\overline{g}^o_{f,i} \equiv \overline{g}^o_i(T) - \sum_{j=1}^{N} \nu'_j \overline{g}^o_j(T) \tag{2.34}$$

$$\Delta G^o_T = (c\overline{g}^o_{C,T} + d\overline{g}^o_{D,T} - a\overline{g}^o_{A,T} - b\overline{g}^o_{B,T}) \tag{2.35}$$

are determined. More importantly, Eq. 2.35 models a reversible reaction of two reactants ($AandB$) and two products ($CandD$) where $\overline{g}^o_f$ is the Gibbs function of formation, ΔG^o_T

is the standard state Gibbs function change, and A-D are the species present with their respective lowercase variables being the stoichiometric coefficients [10]. The values of $\overline{g}_f^o$ are typically tabulated vs temperature for ease of use.

Through more manipulation and defining the equilibrium constant K_p as

$$K_p = \frac{(p_C/p^o)^c (p_D/p^o)^d}{(p_A/p^o)^a (p_B/p^o)^b} \tag{2.36}$$

the equation

$$K_p = \exp(-\Delta G_T^o / R_u T) \tag{2.37}$$

can be found and used to determine the mole fraction $\chi_i = N_i/N_{total}$ of each species using *Dalton's Law of Partial Pressures*.

$$p_i = \chi_i p \tag{2.38}$$

For N species, using Eq. 2.36 and element conservation equations results in a system of $N-1$ equations where $\sum_{i=1}^{N} \chi_i = 1$ is used as the N^{th} equation [10]. Solving this system of equations results in the equilibrium composition of an ideal gas mixture at the given temperature and pressure, allowing for other properties of the gas to be calculated.

2.2.3 Chemical Kinetics and Non-equilibrium

As mentioned in the previous section, the equilibrium state of a combusting system is the state at which the system reaches as $t \to \infty$ regardless of path. That being said, some reactions happen faster than others thus the slower reactions may limit the rate of the faster reactions. Chemical kinetics allows for those rates to be simulated whether they are rate limited or not [10] and will allow the the reactions of a high speed flow to be modelled.

An important value that is attained from kinetics modelling is the forward reaction rate coefficient k_f defined in the modified Arrhenius form as

$$k_f = AT^{\beta} \exp(-\frac{E_A}{R_u T}) \tag{2.39}$$

where A is the collision frequency factor, T is temperature, β is the temperature exponent, and E_A is the activation energy [36]. These values are tabulated for each reaction in the selected mechanism, and then can be used in the *Law of Mass Action* to determine the time rate of change of a species [37].

For the j^{th} species X_j in a given reaction, the *Law of Mass Action* gives the time rate of change of concentration $[X_j]$ as

$$\frac{d[X_j]}{dt} = (\nu_j'' - \nu_j')k_f \prod_{j=1}^{J} [X_j]^{\nu_j'} \tag{2.40}$$

where ν_j'' and ν_j' are the stoichiometric coefficients for the products and reactants respectively and J is the number of species in the reactants of the equation [10]. This gives the rate of change of a species for a singe reaction, which can be extended to the rate of change for a set of reactions by summing the various derivatives. Extending this further for all of the species in a reaction mechanism if I reactions yields the equation

$$\dot{\omega}_j = \sum_{i=1}^{I} (\nu_{j,i}'' - \nu_{j,i}')(k_{f,i} \prod_{j=1}^{J} [X_j]^{\nu_{j,i}'} - k_{r,i} \prod_{j=1}^{J} [X_j]^{\nu_{j,i}''}) \tag{2.41}$$

where $k_{f,i}$ and $k_{r,i}$ are the forward and reverse reaction rate coefficients of the I^{th} reaction and $\dot{\omega}_j$ is a vector of reaction rates for all species in a mechanism [37].

Using Eq. 2.41 gives a system of N ODEs for a mechanism of N species which

can then be used with other ODEs such as those from fluid dynamics as will be seen in the following sections. This forms the basis of the kinetics models used in this work, however, the majority of chemical kinetics math will be handled by an outside solver.

2.2.4 Relevant Canonical Reactors

The combination of chemical kinetics and fluid dynamics exist in many different forms, however, the form selected for this work is a combination of reactors. These reactors use coupled kinetics and fluid dynamics equations to simulate a reacting flow and are able to resolve the changes in a spacial environment. Two reactors utilized in this work are described here, however, there are many other reactor formulations that may be useful for other applications.

Well-Stirred Reactor

The well-stirred reactor (WSR) model describes a constant volume reactor that can be used for flame stabilization studies and have a history of use in the analysis of ramjet combustors [10]. As the name implies, the contents of the WSR are assumed to be perfectly mixed throughout the control volume and to be operating at steady state. As its definition, the WSR is a volume at which the composition instantly changes at the inlet to the outlet values, meaning that the entire volume has the same composition and properties as the outlet except for the inlet [38]. In understanding well-stirred reactor theory, it is helpful to consider Fig. 2.6 which depicts a general control volume of a well-stirred reactor.

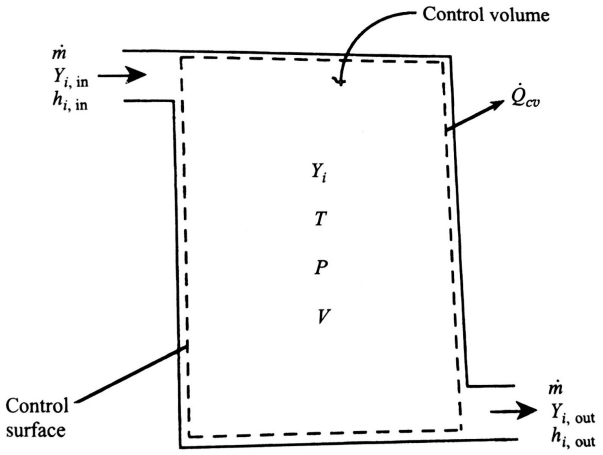

Figure 2.6: Control volume of a well stirred reactor [10]

Starting with mass conservation, the conservation of an arbitrary species i for an integral control volume can be written as

$$\frac{dm_{i,cv}}{dt} = \dot{m}_i''' V + \dot{m}_{i,in} + \dot{m}_{i,out} \tag{2.42}$$

where $\dot{m}_i'''$ is the mass production rate of species i in the given control volume [10]. Considering the chemical kinetics modelling discussed in the previous section, the mass generation rate can be written as

$$\dot{m}_i''' = \dot{\omega}_i MW_i \tag{2.43}$$

where the term $\dot{\omega}_i$ is determined from Eq. 2.41. Assuming the diffusional flux is insignificant, the species mass flow rate can be related to the total mass flow rate using

$$\dot{m}_i = \dot{m} Y_i \tag{2.44}$$

Substituting Eqs. 2.43 and 2.44 into Eq. 2.42 and assuming that the system is

operating at steady state yields the final version of the species mass conservation equation

$$\dot{\omega}_i MW_i V + \dot{m}(Y_{i,in} - Y_{i,out}) = 0 \tag{2.45}$$

which applies to all N species being considered by the mechanism [10].

Considering the conservation of energy for a WSR provides the general steady-state equation

$$\dot{Q} = \dot{m}(h_{out} - h_{in}) \tag{2.46}$$

which can be written in terms of each individual species as

$$\dot{Q} = \dot{m}(\sum_{i=1}^{N} Y_{i,out} h_i(T) - \sum_{i=1}^{N} Y_{i,out} h_i(T_{in})) \tag{2.47}$$

Assuming the system is adiabatic $\dot{Q} = 0$, Eq. 2.47 is then the final energy equation needed to describe the well-stirred reactor. To complete the steady-state formulation, a mean residence time t_R is defined as

$$t_R = \rho * V/\dot{m} \tag{2.48}$$

which is then used with the equation of state and conservation equations to define the flow exiting the reactor [10].

Plug-Flow Reactor

One of the more useful canonical reactors especially in this work is the plug-flow reactor (PFR) which provides a variety of useful simulation capabilities. Namely, it allows for the flow properties to be determined for as a function of x through the integration of a set of ODEs [10, 39] forming an initial value problem that may be applied to a combustor.

From *Turns 1993*, a PFR is defined as an ideal reactor with the following assumptions:

1. Steady-state and steady-flow
2. No mixing/diffusion in the axial direction
3. Uniform properties perpendicular to the flow
4. Ideal frictionless flow
5. Ideal-gas behavior

As with the formulation of the WSR, the PFR is formulated by applying a set of conservation equations to a control volume, which can be see in Fig. 2.7. The conservation

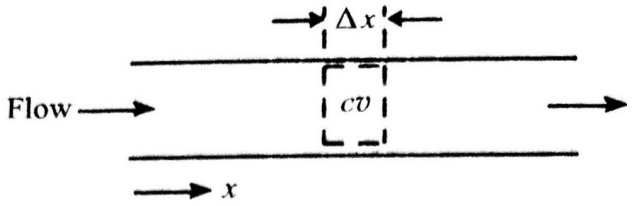

Figure 2.7: Control volume of a plug flow reactor in a duct [10]

equations applied to this differential control volume are that of mass,

$$\frac{d(\rho v_x A)}{dx} = 0 \tag{2.49}$$

momentum in the x-direction,

$$\frac{dp}{dx} + \rho v_x \frac{dv_x}{dx} = 0 \tag{2.50}$$

energy,

$$\frac{d(h + v_x^2/2)}{dx} + \frac{\dot{Q}'' P}{\dot{m}} = 0 \tag{2.51}$$

and lastly species conservation,

$$\frac{dY_i}{dx} - \frac{\dot{\omega} MW_i}{\rho v_x} = 0 \tag{2.52}$$

In addition to these conservation equations, the differential form of the ideal-gas equation of state $P = \rho R_u T / MW_{mix}$ which is

$$\frac{1}{p}\frac{dp}{dx} = \frac{1}{\rho}\frac{d\rho}{dx} + \frac{1}{T}\frac{dT}{dx} - \frac{1}{MW_{mix}}\frac{dMW_{mix}}{dx} \tag{2.53}$$

Defining the mixture molecular weight MW_{mix} as

$$MW_{mix} = [\sum_{i=1}^{N} Y_i / MW_i]^{-1} \tag{2.54}$$

the corresponding derivative with respect to x is then

$$\frac{dMW_{mix}}{dx} = -MW_{mix}^2 \sum_{i=1}^{N} \frac{1}{MW_i}\frac{dY_i}{dx} \tag{2.55}$$

which can then be used in formulating the PFR through Eq. 2.53.

Additionally, defining the enthalpy as a function of temperature and composition $h = h(T, Y_i)$ allows for the enthalpy derivative to be represented by

$$\frac{dh}{dx} = c_p \frac{dT}{dx} + \sum_{i=1}^{N} (h_i \frac{dY_i}{dx}) \tag{2.56}$$

which is then rearranged to solve for the temperature derivative

$$\frac{dT}{dx} = \frac{1}{c_p}(\frac{dh}{dx} - \sum_{i=1}^{N} (h_i \frac{dY_i}{dx})) \tag{2.57}$$

The temperature derivative in Eq. 2.57 is not used for the final temperature derivative, but

is substituted into Eq. 2.53 coupling the change in enthalpy and composition to the density derivative.

While Eqs. 2.49 - 2.55 accurately describe the behavior of a PFR, it is beneficial to reformulate them into directly determine the derivatives of temperature, density, and species mass fraction [10]. Through significant manipulation, the equations for these derivatives are

$$\frac{d\rho}{dx} = \frac{(1 - \frac{R_u}{c_p MW_{mix}})\rho^2 v_x^2(\frac{1}{A}\frac{dA}{dx}) + \frac{\rho R_u}{v_x c_p MW_{mix}} \sum_{i=1}^{N} MW_i \dot{\omega}_i (h_i - \frac{MW_{mix}}{MW_i} c_p T)}{p(1 + \frac{v_x^2}{c_p T}) - \rho v_x^2} \tag{2.58}$$

$$\frac{dT}{dx} = \frac{v_x^2}{\rho c_p}\frac{d\rho}{dx} + \frac{v_x^2}{c_p}(\frac{1}{A}\frac{dA}{dx}) - \frac{1}{v_x \rho c_p}\sum_{i=1}^{N} h_i \dot{\omega}_i MW_i \tag{2.59}$$

$$\frac{dY_i}{dx} = \frac{\dot{\omega}_i MW_i}{\rho v_x} \tag{2.60}$$

which provide most of a system of coupled ODEs that may be integrated over an length in x with an appropriate solver. To complete the system of equations, a residence time t_R is defined

$$\frac{dt_R}{dx} = \frac{1}{v_x} \tag{2.61}$$

The system defined by Eqns. 2.58 - 2.61 may then be solved over a domain using initial conditions for temperature, density, and the species mass fractions while assuming $t_R(0) = 0$ [10].

This completes the mathematical formulation of a PFR and with an ODE solver, the various properties can be solved for as a function of x. The PFR model is a extremely useful tool for capturing the changes in temperature, pressure, and composition in the combustor as they occur across the combustor length. All limitations of the PFR model stem from the assumptions used in its formulation, but it is possible to re-derive the reactor with a different set of assumptions such as removing the frictionless surface assumption.

2.3 Operational Concepts

Described here are the more important concepts and design challenges for scramjet engines that beyond the analysis methods used, are critical to the operation and development of scramjet systems.

2.3.1 Ram-air Compression

The compression mechanism of airbreathing propulsion systems is critical to the performance of the overall system. Ramjet engines are unique from the more popular turbo-jet engines due to their compression method, which is to use the forward velocity of the vehicle to compress the air before it enters the combustor [1] while turbo-jets use a powered compressor. This method is defined as Ram-air compression and is where the Ramjet earned its name.

This compression is achieved through the deceleration of the flow relative to the vehicle, however, as found by Rene Lorin it is not an effective method of compression at lower speeds [1]. Additionally, ram air compression is more useful in supersonic flight [9] where shock waves form and increase the compression going into the inlet of the propulsive device. The design of an inlet for a ram-air device is no easy task, and is outside the scope of this work, but it is necessary to understand the basic function of these devices.

While most ram-air compression occurs on the fore-body and in the inlet, there is significant compression in the isolator ducts of ramjets [1]. This will be shown in the later sections of this work as shock train models are discussed and implemented to simulate the high speed internal flow.

2.3.2 Regenerative Cooling

Due to the nature of high speed flows and combustion, the environment created by this reacting internal flow is hazardous and provides difficulties in designing an engine structure capable of withstanding the high heat loads. A more popular design to handle the heat loads is to use regenerative cooling schemes derived from those used for rocket engines throughout history [20] allowing for the extended firing of scramjet engines.

While regenerative cooling is less effective at speeds at or above Mach 10, it is still one of the more prominent designs in cooling the structure of an engine [40]. Regenerative cooling is not explored in this paper but the work documented here would be the first step in performing studies of engine cooling methods, thus the introduction of the topic here. With a defined flow-path, different cooling channel designs could be considered in order to maximize the possible firing time or the thermodynamic efficiency of the engine.

2.4 Existing 1-D Scramjet Simulation Codes

It is common practice to develop 1-D models for engine development, thus there are many existing simulations similar to the simulation developed here designated CReSS. A handful of models are described here, and the performance trade-offs are considered.

2.4.1 University of Queensland

There has been significant work in scramjet simulation at the University of Queensland, which has led to the creation of a 1-D simulation code similar to the one being developed

here. The Queensland model was described as use a mixing-limited combustion model based on a mixing efficiency curve and the heat release of the selected fuel [13], differing from the reaction rate limiting combustion model used by CReSS. Similar methods are used in both models to account for flow separation, however, the Queensland model was not described to track the changes in chemical composition along the flowpath while CReSS accommodates changes in chemical composition. The final aspect to note of this model is that it is capable of simulating dual-mode combustion but was not shown to simulate a cavity-based flameholder, while CReSS is capable of dual-mode operation and cavity-based flameholders.

2.4.2 VTMODEL

The 2010 VTMODEL was developed to model scramjet and ramjet flowpaths with intended use in "conceptual design and wind tunnel testing" and is capable of acting as a analysis tool as well as a predictive model [41]. Similar to the model developed here, VTMODEL breaks the engine into components based on canonical stations and accounts for the various interactions between components. A drawback of the VTMODEL is that it requires an input pressure for either the combustor entrance, combustor exit, or nozzle exit [41], which can be prohibitive when it is being used in a predictive manner. This work attempts to address this shortcoming with a number of assumptions addressed later.

VTMODEL has two different combustion models available, one of which being a "growing combustion sphere" model and the other being a non-equilibrium kinetics model similar to the one used by CReSS [41]. CReSS is limited to the non-equilibrium kinetics model and as a result is reaction rate limited. At its state after initial development the VTMODEL was only usable for hydrogen fuel and omits flow separation, both of which are improvements that the model developed improves upon. A major focus that the newly

developed model addresses is simulating non-equilibrium flow that crosses the sonic line. Due to a $(1 - M^2)$ term in the denominator and the resulting division by zero at $M = 1$, the VTMODEL is limited to pure subsonic or pure supersonic combustion and is thus incapable of simulating dual-mode conditions [41].

2.4.3 Birzer and Doolan's Model

A 1-D simulation is discussed in *Birzer and Doolan, 2009* at the University of Adelaide which models a hydrogen-fueled scramjet combustor using mixing-limited combustion chemistry. The "mixed is burned" combustion assumption is completed using a mixing model along with an equilibrium chemistry model [42], a different approach to combustion modeling than the model developed here which uses kinetics to form a reaction-rate limited combustion model. *Birzer and Doolan's* model has been validated for pure supersonic combustion with wall or ramp fuel injectors, however, was not validated for dual-mode operation or cavity-based flameholders.

2.4.4 SUNDIALS

Developed by the Harbin Institute of Technology, the SUNDIALS simulation code was developed specifically to model a scramjet combustor with regenerative cooling and captures some of the heat transfer between the flow and combustor walls. The SUNDIALS model includes a mixing model as well as heat transfer model for the flow which requires additional equations to be solved with the flow simulation, which is done through iterating on the fuel injection conditions and closing the simulation using a residual from the flow and cooling tube model [20]. The SUNDIALS simulation is not explicitly stated to model cavity-

based flameholders and uses a mixing controlled chemistry model as opposed to a kinetics limited model [20]. CReSS uses a kinetics limited combustion mode, and was developed with a focus on simulating cavity-based flameholders.

Chapter 3

Formulation and Validation of Engine Analysis Code

Delving into the simulation efforts of this work, this chapter discusses and catalogs the various analysis methods considered and the reasons for those selected. Additionally, the interaction of each system component is described and the overall scramjet simulation is compared against the data of previous studies.

3.1 Engine Component Breakdown

The work described here, as well as other studies, approaches the task of engine simulation by breaking up the engine into general components and considering the interactions between them. Engine components considered in this work comprise of the isolator-duct, the combustor, and the expansion exhaust nozzle. Before moving forward with each component, it is important to describe the overall system arrangement and put forth the notation used for key locations in the system. For hypersonic vehicles, these key locations, or stations, are defined by the following diagram which uses a typical wave-rider geometry similar to that of the X-43 and X-51 flight vehicles [43].

As seen in Fig. 3.1, the canonical stations include flow upstream and downstream

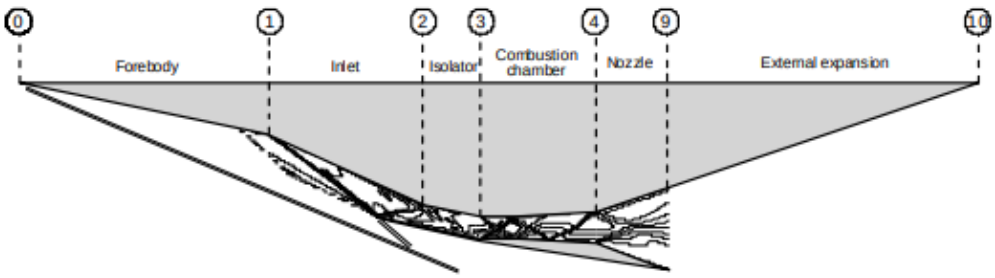

Figure 3.1: Diagram of flow stations for an air-frame integrated scramjet [11]

of the propulsion system in addition to the internal flows. Due to the inherent 2-D nature of external flows, they will be excluded from this analysis. This reduces the areas of analysis from stations 0-10 down to stations 2-6 spanning the isolator compression system, the combustor, and the nozzle. The remaining portions of this section detail the methods used for each of these three components.

To assist in the development and validation of the flowpath analysis code, the geometry and supporting studies from the HIFiRE program are used. From the flowpath development process described in *Gruber 2008*, the HIFiRE simulation geometry that will be used can be seen in Fig. 3.2 and the coordinates for the listed points are found in Fig.

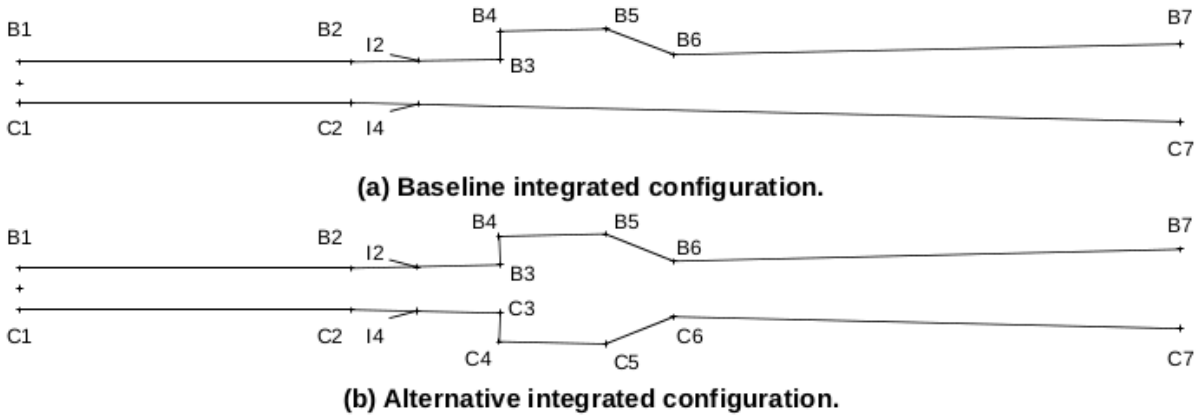

Figure 3.2: Isolator/combustor flowpath diagram for HIFiRE experiments [12]

3.3.

	Baseline		Alternative	
	x [mm (in.)]	*y* [mm (in.)]	*x* [mm (in.)]	*y* [mm (in.)]
C1	0.000	-12.7 (-0.500)	0.000	-12.7 (-0.500)
C2	203 (8.000)	-12.7 (-0.500)	203 (8.000)	-12.7 (-0.500)
C3	-	-	295 (11.596)	-14.8 (-0.582)
C4	-	-	294 (11.581)	-31.9 (-1.256)
C5	-	-	359 (14.150)	-33.4 (-1.315)
C6	-	-	401 (15.794)	-17.2 (-0.677)
C7	711 (28.003)	-24.2 (-0.954)	711 (28.003)	-24.2 (-0.954)
B1	0.000	12.7 (0.500)	0.000	12.7 (0.500)
B2	203 (8.000)	12.7 (0.500)	203 (8.000)	12.7 (0.500)
B3	295 (11.596)	14.8 (0.582)	295 (11.596)	14.8 (0.582)
B4	294 (11.581)	31.9 (1.256)	294 (11.581)	31.9 (1.256)
B5	359 (14.150)	33.4 (1.315)	359 (14.150)	33.4 (1.315)
B6	401 (15.794)	17.2 (0.677)	401 (15.794)	17.2 (0.677)
B7	711 (28.003)	24.2 (0.954)	711 (28.003)	24.2 (0.954)
I2	244 (9.596)	13.6 (0.536)	244 (9.596)	13.6 (0.536)
I4	244 (9.596)	-13.6 (-0.536)	244 (9.596)	-13.6 (-0.536)

Figure 3.3: HIFiRE flow path coordinates [12]

This 2D geometry was selected as it has a cavity requiring the simulation of re-circulation regions, as well as multiple cases which to compare the model. The geometry also has secondary fuel injection points downstream of the cavity, however, those will not be considered in this work. The geometry is first discretized into a series of points that define its cross-section, as seen in Fig. 3.4

The points plotted in Fig. 3.4 will be those that flow-path data is recorded and are prescribed at the beginning of the analysis. It should be noted that the more points considered for analysis, the more computational time will be required.

3.1.1 Inlet/Isolator

As mentioned above, this work begins its analysis at the entrance to the isolator defined as station 2 in 3.1. These components typically consist of an internal flow compression component upstream of the combustor, and uses a train of shock waves to generate a pressure rise [1]. While these shock trains and pressure generation are critical to the operation of

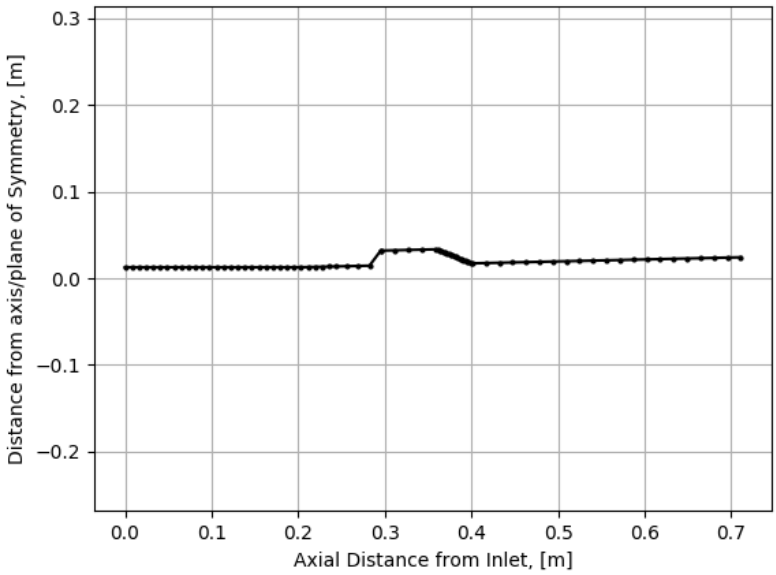

Figure 3.4: Discretized engine flow-path boundary

scramjets, it is important that the isolator duct is sized correctly to contain the shock train. In the case that the leading shock extends upstream of station 2, the inlet may unstart and lead to an engine flame-out [1].

The analysis of the isolator component is split into two parts: one that analyzes the flow upstream of the shock train, and one for the flow within the shock train. Upstream of the leading shock, the flow is modeled as a viscous, adiabatic supersonic internal flow, and is assumed to be attached. Additionally, it is assumed to be in chemical equilibrium reducing the computational requirements.

Before analyzing the flow of the isolator, it is necessary to determine the leading edge of the shock-train. To find this, the empirical relation

$$\frac{s_t(M_2^2-1)Re_\theta^{1/4}}{D^{1/2}\theta^{1/2}} = 50(\frac{p_3}{p_2}-1)+170(\frac{p_3}{p_2}-1)^2 \tag{3.1}$$

from *Waltrup and Billig, 1973* is employed for circular ducts, and the modified version

$$\frac{s_t(M_2^2-1)Re_\theta^{1/5}}{H^{1/2}\theta^{1/2}} = 50(\frac{p_3}{p_2}-1)+170(\frac{p_3}{p_2}-1)^2 \tag{3.2}$$

is used for rectangular ducts [44]. In Eqns. 3.1 and 3.2, D and H represent the duct diameter and duct height, respectively, while the subscripts $2, 3$ represent the canonical stations represented in Fig. 3.1. While at the beginning of the analysis only p_2 is known, through a procedure described in a following section it is possible to obtain an estimate of p_3 for use with the shock train equations.

Upstream of the shock train, the flow is considered to be a viscous, adiabatic flow, meaning that there is an entropy gain due to viscous forces, but there is no change in the total enthalpy. With these assumptions, the differential conservation equations needed are Eqs. 2.20, 2.21, and 2.22, which can be re-arranged to yield the equations

$$\frac{dp_0}{p_0} = -\frac{\gamma M^2}{2}\frac{dT_0}{T_0} - \frac{\gamma M^2}{2}\frac{4C_f dx}{D} \tag{3.3}$$

$$\frac{dM^2}{dx} = M^2[1+\frac{\gamma-1}{2}M^2]\frac{[-\frac{2}{A}\frac{dA}{dx}+(1+\gamma M^2)\frac{1}{T_0}(\frac{dT_0}{dx})+4\gamma m^2 C_f/D]}{1-M^2} \tag{3.4}$$

taken from *Hill and Peterson, 1992*. With these two equations as well as the adiabatic and chemical equilibrium assumptions, it is now possible to iterate the temperature and pressure at each axial location of interest and close upon a solution.

A single iteration solving for the i^{th} axial location begins with guessing temperature and pressure values, typically close to those of the previous axial location, $(i-1)$. These, along with the species mole fractions, are then used to determine the equilibrium composition using a nonlinear PDE solver such as Cantera [45]. With Cantera, the axial location is equilibrated at the prescribed temperature and pressure, yielding the density ρ, molecular

weight MW, and more. Using the adiabatic assumption,

$$h_t = h_{i-1} + \frac{v_{x,i-1}^2}{2} = constant = h_i + \frac{v_{x,i}^2}{2} \tag{3.5}$$

which using equilibrium chemistry to solve for h at the new axial location allows for Eq. 3.5 to be rearranged as

$$v_{x,i} = \sqrt{2(h_t - h_i)} \tag{3.6}$$

Since the flow is adiabatic, h_t is known from the previous axial location yielding the velocity at the i^{th} location. Using the newly calculated velocity and current values of temperature and pressure, it is now possible to calculate the derivatives in Eqns. 3.3 and 3.4 using finite difference methods. For this problem, a backwards difference method was applied in the form of

$$\frac{df(x_i)}{dx} = \frac{f(x_i) - f(x_{i-1})}{x_i - x_{i-1}} \tag{3.7}$$

where f represents any function of x [46], which in this case will be flow parameters such as temperature.

With the derivatives calculated, it is now possible to calculate the values of Eqs. 3.3 and 3.4, forming a system of equations solvable by a nonlinear system of equations solver similar to *fsolve* in MATLAB or Python's Scipy library. This process is then iterated until the system is within the set tolerances before moving on to the next axial location. For the isolator, this process occurs until all of the axial locations have been calculated or until the system steps past the leading edge of the shock train whose length is determined with one of Eqs. 3.1 and 3.2. Due to the separation which occurs within the shock train, a different simulation method is employed.

Shock Train Analysis

While Eqns. 3.1 and 3.2 provide the shock leading edge, it does not provide the means to simulate the flow within the shock train. As shown by Fig. 3.5 the flow separates

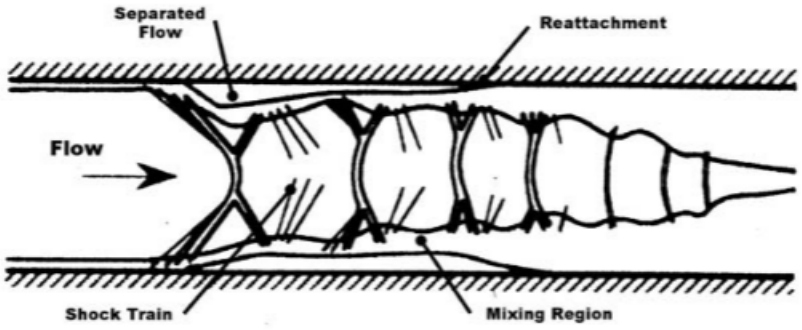

Figure 3.5: Schematic of flow structure in an isolator duct, [13]

downstream of the shock resulting in a multi-stream flow providing a complex flow system. The complexities of the system make it difficult to capture the flow-field in a one-dimensional code, thus multiple relations both theoretical and empirical have been created to provide the pressure distribution within the shock train.

One such relation can be found from *Weiss, 2010*

$$\frac{p - p_2}{p_3 - p_2} = \frac{(w_2^2(w_2^2 - 2w^{*2}) + w_2^2 w^{*2} e^{-c(x/D)})(1 - e^{-c(x/D)})}{(w_2^2 - w^{*2})^2 - w_2^2(w_2^2 - w^{*2})e^{-c(x/D)}(1 - e^{-c(x/D)})} \tag{3.8}$$

which describes the pressure p at for a given x distance past the shock wave. In this equation, c is an empirical constant of 0.114, w is the Crocco number, and w^* is the Crocco number at sonic conditions [44]. For a given flow, the Crocco number is defined as

$$w = u/\sqrt{2c_p T_t} \tag{3.9}$$

and the Crocco number at sonic condition can be written as

$$w^* = \sqrt{(\gamma - 1)/(\gamma + 1)} \tag{3.10}$$

which completes a system of equations to determine the static pressure profile over the length of the shock train.

With the pressure profile known, it is now possible to determine the rest of the one-dimensional flow within the shock train through manipulation and integration of the differential conservation equations. It is important to note that during shock train formation, the flow within it separates, introducing another variable which will be regarded as the core flow area A_c. A differential element, or finite element, that the conservation equations are applied to typically looks like that in Fig. 3.6. The conservation equations are then integrated across the control volume and control surfaces.

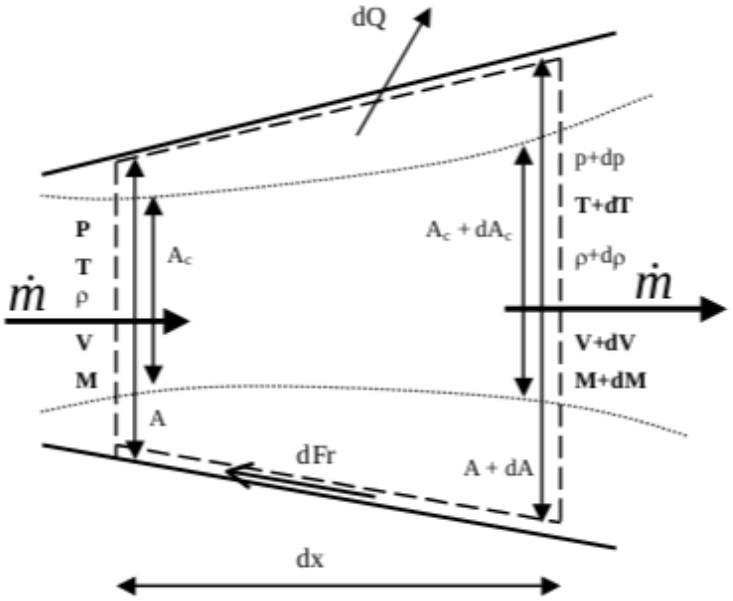

Figure 3.6: Differential element of separated flow, [13]

Following the analysis in *Smart 2010*, the conservation of mass, momentum and energy applied to the control volume depicted in Fig. 3.6 yields the equations

$$\frac{d\rho}{\rho} + \frac{dV}{V} + \frac{dA_c}{A_c} = 0 \tag{3.11}$$

$$\frac{dp}{p} + \frac{\gamma M^2}{2}\frac{4C_f dx}{D_h} + \frac{\gamma M^2}{2}\frac{A_c}{A}\frac{dV^2}{V^2} = 0 \tag{3.12}$$

$$\frac{dT}{T} + \frac{\gamma - 1}{2}M^2\frac{dV^2}{V^2} = (1 + \frac{\gamma - 1}{2}M^2)\frac{dT_t}{T_t} \tag{3.13}$$

Applying the adiabatic assumption, $dT_t/dx = 0$ and performing some algebraic manipulation, the equations become

$$d\rho = -\rho(\frac{dV}{V} + \frac{dA_c}{A_c}) \tag{3.14}$$

$$dV^2 = -V^2\frac{(\frac{dp}{p} + \frac{\gamma M^2}{2}\frac{4C_f}{D_h})}{\frac{\gamma M^2}{2}\frac{A_c}{A}} \tag{3.15}$$

$$\frac{dT}{T} + \frac{\gamma - 1}{2}M^2\frac{dV^2}{V^2} = 0 \tag{3.16}$$

which produces a solvable system when applying a pressure distribution such as the one described in Eq. 3.8. This set of four equations are then integrated over the length of the shock train completing the flow analysis of the engine's isolator once the pressure at station 3 is determined.

Isolator-Burner Interaction

In order to determine the pressure at the combustor entrance, the interaction between the isolator and burner must be considered. If examined separately from the other

engine components, the isolator acts as a back pressured nozzle [1, 47]. This reinforces the necessity of a method to accurately determine the pressure at the burner entrance which will give the last piece of information for the isolator.

Following a method described in *Heiser and Pratt, 1994*, the pressure at the burner entrance is determined by a two-step process. The first step is to analyze the isolator as a shock-free duct which provides the solution of no flow separation. These results are then used to simulate the combustor, where the location of the highest pressure is referred to as Station s. If at this point the local Mach number is less than 0.762 M_2, the flow is assumed to separate.

The method of the second step is dependent on this separation: if the flow *does not* separate, the isolator is assumed to be shock free and the engine operates as a pure scramjet. If the flow *does* separate, the maximum pressure of the shock free burner is used as the isolator back pressure p_3 and a shock train is assumed to form in the isolator. Additionally, it is then assumed that the combustor operates at constant pressure throughout [1].

3.1.2 Combustor

Comprising of multiple sub-units in itself, the combustor is typically defined as the component between stations 3 and 4. Located at the entrance of the combustor are fuel injectors, of which there are many configurations. Following fuel injection is a mixing length and/or a cavity-based flame-holder, which creates re-circulation regions to improve flame-holding capability. These sub-components are then followed by a diverging duct leading to the expansion nozzle.

As seen in Fig. 3.2, the HIFiRE geometry has a cavity-based flame-holding device

necessitating a separation/re-circulation zone model. Due to the 1-D nature of the flow simulation in this work and the higher dimension nature of separation zones, the core flow areas in the cavity are prescribed based on the core flow entering the cavity and the wall geometry. This is shown to yield relatively accurate simulations without significantly increasing computational requirements.

Flame-holding and Fuel Injection

Scramjet fuel injection is an expanding field for research as it is critical to combustor operation and there are a number of fuel injection methods. Commonly seen are wall-injectors, ramp injectors, and strut mounted injectors [1] each having their own respective benefits. Effective injection and mixing is critical as hydrocarbon-based scramjets see unique difficulties stemming from slow overall kinetic rates and short combustor residence times due to the high speeds [48].

As documented in *Gruber, 2008* the HIFiRE geometry uses wall injectors normal to the wall and burns ethylene fuel C_2H_4. This is important to the fuel-injection method as injectors normal to the wall do not add any momentum in the axial direction. With this knowledge, a mass, momentum, and energy balance is used at the point of fuel injection assuming none of the fuel has reacted.

Holding flame in a scramjet combustor is no easy task due to the time scales issues mentioned earlier in this section, however, the wall-based cavity of the HIFiRE geometry reduces this challenge greatly. To assist in the combustion modeling and to account for the mixing immediately downstream of fuel injection it is assumed that the fuel does not start reacting until entering the cavity.

Cavity Shock Wave Formation

Discussed previously in Sec. 2.1.2, when a supersonic flow encounters a turn, an oblique shock forms causing a variety of changes. As a result of the potential for supersonic flow in the cavity, at the end of which there is often a corner in the engine surface that reduces the cross-section down to a choke point. In the case that the cavity is supersonic, a shock wave will form in this area of the engine whose strength is dependent on the geometry of the cavity. Such shock waves can be seen in Fig. 3.7 which depicts the unsteady nature of flat rear wall cavities and the stabilization benefits of a ramped rear wall [14].

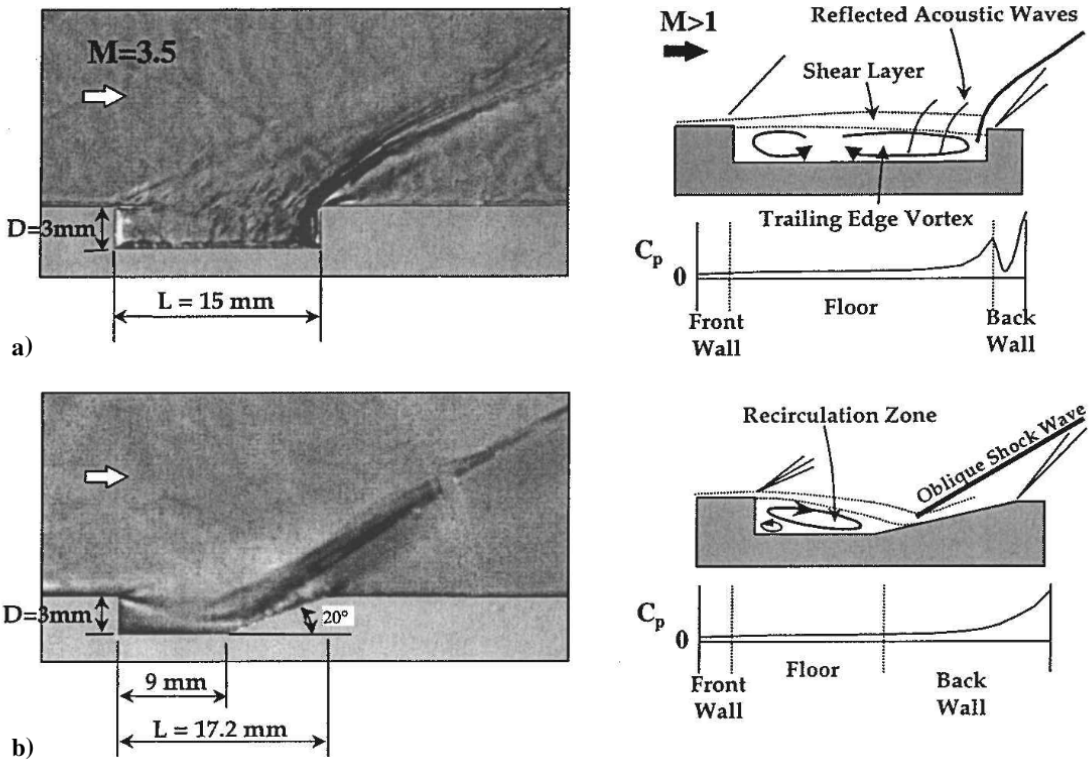

Figure 3.7: A set of Schlieren images taken of supersonic cavities and corresponding diagrams showing the effect cavity geometry has on the flow: a) cavity with perpendicular back wall leading to acoustic instabilities and b) a slanted back wall cavity stabilizing the flow reattachment process [14]

To include these shock waves in the simulation is not a difficult task, however, it must be done with care as the cavity is not always supersonic. It was decided to apply a set of conditions that if all are met, a shock is assumed to form. These conditions are:

- The flow is supersonic
- The cross-sectional area is decreasing
- There has not been a shock wave in the cavity already

Once a shock wave is assumed to form, the turning angle δ is calculated from the geometry and then a shock wave angle σ is iterated until the Eq. 2.18 is solved. Once σ is obtained, the normal and tangential velocity components are calculated and Eqs. 2.14 - 2.17 are solved. The results of this calculation are then used to solve the Constant Pressure Plug Flow Reactor which is defined in Sec. 3.2.

The Need for Non-equilibrium Methods

As mentioned in previous sections, this work discusses two different methods of combustion analysis: equilibrium chemistry and finite-rate chemical kinetics. While equilibrium chemistry is much quicker to calculate, the high velocity flow inside scramjet engines typically have residence times too short to reach equilibrium [1]. Due to the similar time scales of the supersonic flow and chemical reactions, it is often more accurate to model the combustion using finite-rate chemistry.

One-Dimensional System of Reactors

In this work, the combustor is modeled as a series of canonical reactors which model not only the temperature, pressure, and velocity of the flow, but models the chemical changes as the fuel-air mixture reacts. Namely, the combustor model described here is a series of Well-Stirred and Plug Flow reactors in a configuration similar to that seen in Fig. 3.8.

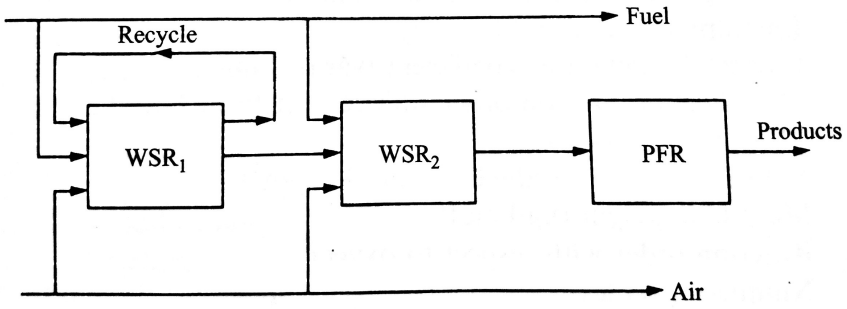

Figure 3.8: Conceptual model of a gas-turbine combustor using a series of canonical reactors, [10]

While the model in Fig. 3.8 is for a gas-turbine combustor, a similar arrangement can be created for a ramjet/scramjet combustor. Such an arrangement, and the arrangement used to match the HIFiRE studies previously mentioned, is represented in Fig. 3.9.

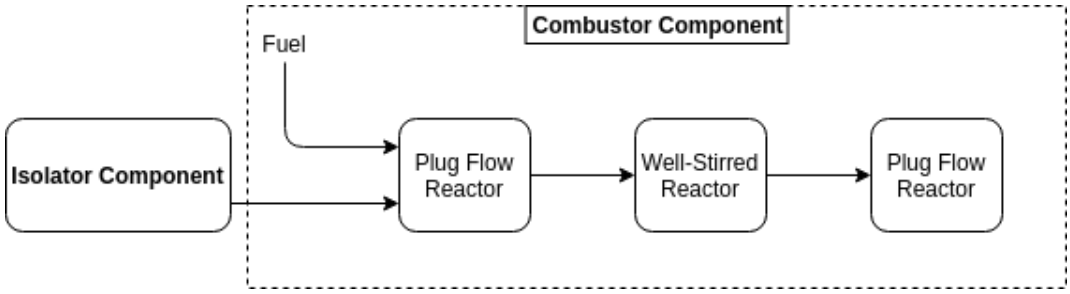

Figure 3.9: Series of reactors used to model the HIFiRE system

It should be noted that while the order of reactors is different than the gas-turbine

model from *Turns, 2000*, the concept of using a network of smaller reactors to model a larger combustion system remains the same. Additionally, the Well-Stirred Reactor's location is at the beginning of the HIFiRE cavity, helping enforce the non-reacting "mixing zone" between fuel injection and cavity.

3.1.3 Nozzle

After the combustor, the flow enters an expansion nozzle designed to accelerate the flow. There are a number of ways to analyze the nozzle, however, this work models it using a Plug-Flow Reactor allowing for the reacting flow to be tracked from the beginning of the combustor through the end of the nozzle. It should be noted that the model discussed here is for internal flows and thus does not extend past station 9, and the HIFiRE geometry does not extend past station 4.

3.2 Plug-Flow Reactor(PFR) Revisited

As with all analyses, it is important to address the shortcomings of the methods implemented and attempt to remedy them. In the plug flow reactor derivation, it is assumed that friction is negligible which allows for the use of the Euler momentum equation [10], however, here the PFR will be re-derived without that assumption. The derivation of the modified PFR starts with the conservation equations

$$\frac{d(\rho v_x A)}{dx} = 0 \tag{3.17}$$

$$\frac{dp}{dx} + \rho v_x \frac{dv_x}{dx} = -\frac{\tau_0 c}{A} \tag{3.18}$$

$$\frac{d(h + v_x^2/2)}{dx} + \frac{\dot{Q}''c}{\dot{m}} = 0 \tag{3.19}$$

$$\frac{dY_i}{dx} - \frac{\dot{\omega}_i MW_i}{\rho v_x} = 0 \tag{3.20}$$

where the difference between these and those from the original PFR derivation is the shear force τ_0 term in Eq. 3.18 which is taken from *Hill and Peterson* [9]. As with the previous derivation, the system is assumed to be adiabatic thus $\dot{Q}'' = 0$.

To help non-dimensionalize and make the momentum term more useful, a friction coefficient $C_f = \tau/(\frac{1}{2}\rho v_x^2)$ is employed and is later determined using one of the many functions of the form $C_f = f(Re)$. Implementing the friction coefficient and with some rearranging, Eq. 3.18 becomes

$$\frac{dp}{dx} = -\rho v_x \frac{dv_x}{dx} - \frac{1}{2}\rho v_x^2 \frac{4C_f}{D} \tag{3.21}$$

where D is the diameter of the differential element.

The pressure derivative in Eq. 3.21 as well as the temperature derivative in Eq. 2.57 are then substituted into the differential *Equation of State* given by Eq. 2.53 yielding the equation

$$\frac{1}{p}(-\rho v_x \frac{dv_x}{dx} - \frac{\rho v_x^2}{2}\frac{4C_f}{D}) = \frac{1}{\rho}\frac{d\rho}{dx} + \frac{1}{T}\frac{dT}{dx} - \frac{1}{MW_{mix}}\frac{dMW_{mix}}{dx} \tag{3.22}$$

which is then rearranged to obtain the density derivative

$$\frac{d\rho}{dx} = \rho v_x \frac{dv_x}{dx}(\frac{1}{c_p T} - \frac{\rho}{p}) - \frac{1}{2}\rho^2 v_x^2 \frac{4C_f}{pD} + \frac{\rho}{Tc_p}\sum_{i=1}^{N}[h_i \frac{dY_i}{dx}] + \frac{\rho}{MW_{mix}}\frac{dMW_{mix}}{dx} \tag{3.23}$$

Before further manipulation of Eq. 3.23, Eq. 3.17 is expanded to give

$$\frac{1}{\rho}\frac{d\rho}{dx} + \frac{1}{v_x}\frac{dv_x}{dx} + \frac{1}{A}\frac{dA}{dx} = 0 \tag{3.24}$$

and rearranged to get

$$\frac{dv_x}{dx} = v_x(-\frac{1}{\rho}\frac{d\rho}{dx} - \frac{1}{A}\frac{dA}{dx}) \tag{3.25}$$

The velocity derivative in Eq. 3.25 is then substituted into Eq. 3.23 along with Eq. 2.55. After significant algebra, the final density derivative is found to be

$$\frac{d\rho}{dx} = \frac{(1 - \frac{R_u}{c_p MW_{mix}})\rho^2 v_x^2(\frac{1}{A}\frac{dA}{dx}) - \frac{\rho^2 v_x^2}{2}\frac{4C_f}{D} + \frac{\rho R_u}{v_x c_p MW_{mix}}\sum_{i=1}^{N} MW_i\dot{\omega}_i(h_i - \frac{MW_{mix}}{MW_i}c_pT)}{p(1 + \frac{v_x^2}{c_pT}) - \rho v_x^2} \tag{3.26}$$

where the term with C_f in the numerator accounts for the friction from the walls.

The friction only affects the energy term through the density derivative that appears in the equation for temperature derivative

$$\frac{dT}{dx} = \frac{v_x^2}{\rho c_p}\frac{d\rho}{dx} + \frac{v_x^2}{c_p}(\frac{1}{A}\frac{dA}{dx}) - \frac{1}{v_x\rho c_p}\sum_{i=1}^{N} h_i\dot{\omega}_i MW_i \tag{3.27}$$

As done with the original PFR derivation, a derivative of residence time is employed

$$\frac{dt_R}{dx} = \frac{1}{v_x} \tag{3.28}$$

providing a third ODE. In order to determine the enthalpies and mixture properties, the mixture composition is tracked by rearranging 3.20 to be

$$\frac{dY_i}{dx} = \frac{\dot{\omega}_i MW_i}{\rho v_x} \tag{3.29}$$

allowing for the changing species mass fractions to be tracked throughout the length of the reactor [10]. This fourth differential equation completes the system of equations defining the Viscous Plug-Flow Reactor (VPFR) which will be used to simulate the flow throughout the combustor and nozzle.

In addition to the VPFR, another PFR variant is derived here for the constant pressure burner discussed in Sec. 3.1.1, which will be referred to as a Constant Pressure PFR, or CPPFR. By setting $dp/dx = 0$, the differential *Equation of State* in Eq. 2.53 can be rearranged to be

$$\frac{d\rho}{dx} = \frac{-\frac{\rho v_x^2}{Tc_p}\frac{1}{A}\frac{dA}{dx} + \frac{1}{Tc_p v_x}\sum_{i=1}^{N}\dot{w}_i MW_i(h_i - \frac{MW_{mix}}{MW_i}Tc_p)}{1 + \frac{v_x^2}{Tc_p}} \tag{3.30}$$

This density derivative, along with Eqs. 3.20, 3.27, and 3.28 can then be integrated along the axial length of the reactor, completing the CPPFR derivation. The CPPFR will be used for the length of the engine between the fuel injectors and the contraction of the cavity end, at which the VPFR will be implemented. For all reactors discussed in this paper, many properties, namely the species production rates, are solved using the open source kinetics solver Cantera [45].

Before moving forward with the application of these reactors in the combustor model, it is necessary to identify their assumptions, limitations and appropriate use cases. The assumptions used for deriving the VPFR are

1. Steady-state and steady-flow

2. No mixing/diffusion in the axial direction

3. Uniform properties perpendicular to the flow

4. Ideal-gas behavior

which are the same as listed in 2.2.4 without the assumption of *Ideal frictionless flow*. Another assumption must be made when selecting the appropriate C_f equation which is dependent on the flow regime being simulated. For this work, the equation

$$C_f = 0.046(Re_D)^{-1/5} \tag{3.31}$$

from *Hill and Peterson* is employed to determine the appropriate friction coefficients. It should be noted that Eq. 3.31 assumes that the flow is turbulent, and is a good fit for $3x10^4 < Re_D < 10^6$ [9]. With these assumptions in mind the combustor model can now be assembled, concluding the formulation of the Canonical Reactor Scramjet Simulation (CReSS).

3.3 HIFiRE Validation Cases

With the system model described, it is necessary to verify and validate the model with either test data or higher fidelity simulations. This section validates the discussed model through comparison with CFD studies of the HIFiRE geometry, specifically cases where the engine is operating near the transition point from dual-mode ramjet to pure scramjet. It should be noted that since the data used for this validation is from another simulation rather than experiments, the validation of the model is partially complete. Further validation of CReSS should be done with experimental data and various geometries.

Unlike the validation, a informal verification was performed at a component scale; the standard PFR and WSR simulations were compared against other canonical reactor

codes, the shock calculations were compared with the contours in Fig. 2.5, and the flow with friction models were compared with similar codes. A component level verification was selected as similar simulations are typically not readily available.

Before moving forward, it is necessary to discuss the characteristics of the two cases regarding the equivalence ratio and inlet conditions, which are cataloged in Table 3.1. It should be noted that both cases use an equivalency ratio ϕ of unity with an ethylene C_2H_4 and methane CH_4 mixture as fuel which is intended to replicate the properties of "partially cracked" JP7. More specifically, the fuel mixture used is 64% C_2H_4 and 36% CH_4 by volume [12], and the inlet air mixture is assumed to consist of 3.76 moles of N_2 for each mole of O_2, which is a widely used estimate for air [10].

Table 3.1: Inlet conditions for HIFiRE CFD comparisons, [12]

Case	M_2	p_2, [kPa]	T_2, [K]	ϕ
1	2.95	125	786	1.0
2	3.40	100	786	1.0

With the model constructed and the comparison cases defined, a comparison between the model described here and the well validated Vulcan CFD used for the HIFiRE studies. Seen in Figs. 3.10 and 3.11 are the results of the Vulcan CFD reduced to 1-D profiles along with the corresponding results from the CReSS model defined earlier in this chapter. The reduction of data from 3-D to 1-D was performed using a "separated-flow averaging technique" which uses two distortion terms while preserving mass, momentum, and energy profiles in addition to the pressure and kinetic energy profiles. Integrating the CFD solution produces a set of variables, namely total energy flow and pressure force, which are then used with the areas to determine average static pressure, enthalpy, and velocity terms at axial locations spanning the engine [12].

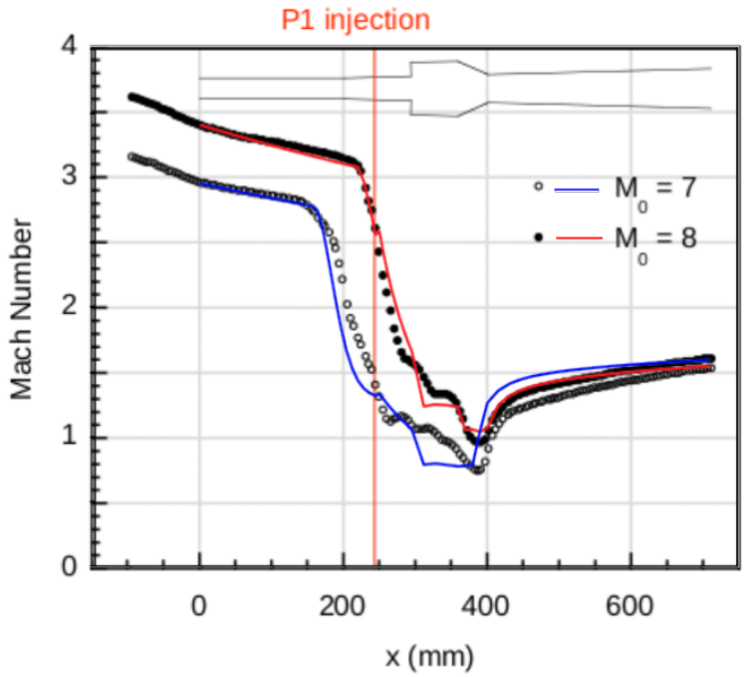

Figure 3.10: HIFiRE Vulcan simulation 1-D Mach number profile [12] with CReSS results in blue(Case 1) and red(Case 2)

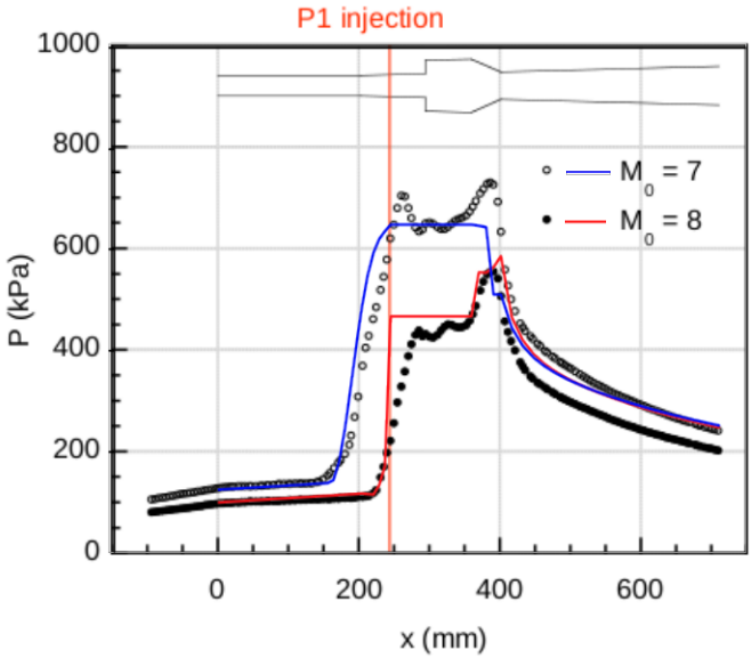

Figure 3.11: HIFiRE Vulcan simulation 1-D pressure profile [12] with CReSS results in blue(Case 1) and red(Case 2)

Considering Case 1, it is seen that the shock train length determined by CReSS is in agreement with that of the Vulcan data, however, it is also shown that the pressure (and Mach) profiles within the shock train do not match fully. At first glance Case 2 has a similar behavior with the elevated pressure values immediately downstream of the P1 injection point, but upon consideration of how CReSS was formulated it is far more likely that it is the result of an assumption made about the burner. More specifically, in Sec. 3.1.1 it was assumed that if the flow separates in the burner the entire burner was to operate at constant pressure. As shown by the HIFiRE data, this assumption is not entirely accurate.

Downstream of fuel injection, CReSS and the Vulcan results have excellent agreement for the supersonic flow of Case 2, but the same cannot be said for Case 1. As shown by Fig. 3.10, the Mach number determined by CReSS for Case 1 is under predicting for the forward portion of the combustor, then goes supersonic at a point upstream of where the Vulcan results predict. Additionally, the flow in the aft combustor portion($400 < x < 700$ mm) should be at a lower Mach number in Case 1 than in Case 2, but this is not the case.

The pressure profiles have a similar story, however they do follow similar trends as the Vulcan profiles with some notable differences. The Case 1 profile does not capture the increased pressure distributions just downstream of fuel injection nor does it capture the pressure rise at the end of the cavity. To the contrary, the pressure drops suddenly at the end of the cavity which prompts the idea that the integration may not have the correct step-size in that region. This was considered and it was found that a refined step size does not change the results. The model does however match the aft combustor profile with some accuracy however does under predict the pressure at the very beginning. This under-prediction is likely a result of not having the raised pressure at $x = 400$ mm. Case 2 tells a different story, and has good agreement with the reduced Vulcan data up until the end of the cavity.

While CReSS does not match the HIFiRE data perfectly, it should be noted that CReSS is a low fidelity model created with the goal of reducing computational requirements, thus the accuracy of results is traded for rapid aero/thermodynamic analysis. With run times on the order of seconds, CReSS achieves this goal with significant accuracy, where 3D CFD models often have computational times on the order of hours depending on the size and fidelity.

Downstream of the cavity, the model loses its agreement and does not capture the pressure drop shown in Fig. 3.11. The changes near the end of the cavity for both cases are concerning and warrant further investigating as capturing the flow near the sonic point is necessary for further modeling. To ensure that the adiabatic assumption is being fulfilled, the static and total enthalpies were plotted in Fig. 3.12.

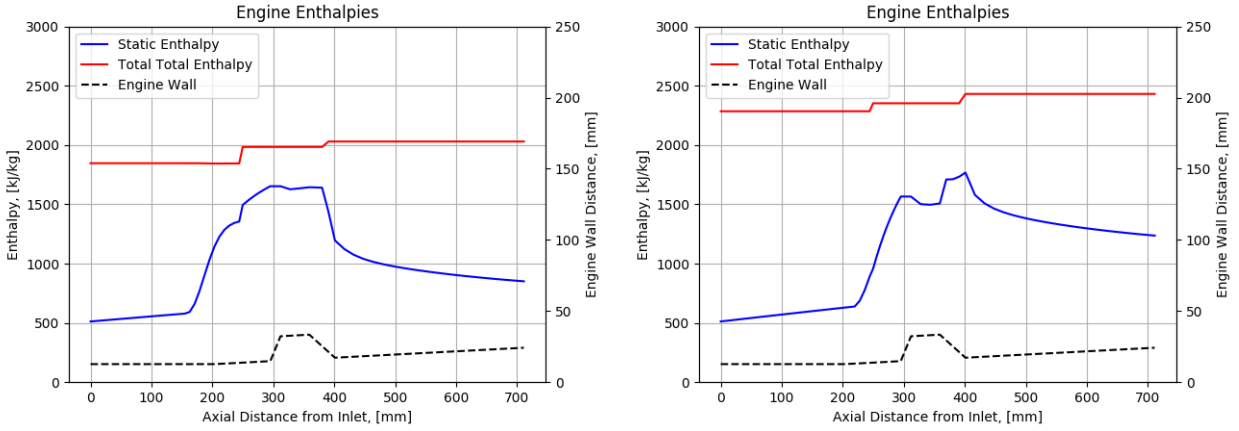

(a) Case 1 enthalpy values

(b) Case 2 enthalpy values

Figure 3.12: Static and total enthalpy values from CReSS evaluation of selected HIFiRE cases

Considering Fig. 3.12, it is seen that there are two sudden increases in total enthalpy, the first of which is fuel injection where the enthalpy of the fuel is added to the flow. The jump near x=400 mm, however, is aberrant, thus the formulated model is in violation of the adiabatic assumption near the choke point. Further investigating this spike, the total

pressure profiles were plotted with markers to show the locations of individual data points to aid in finding the location where the simulation's behavior changes.

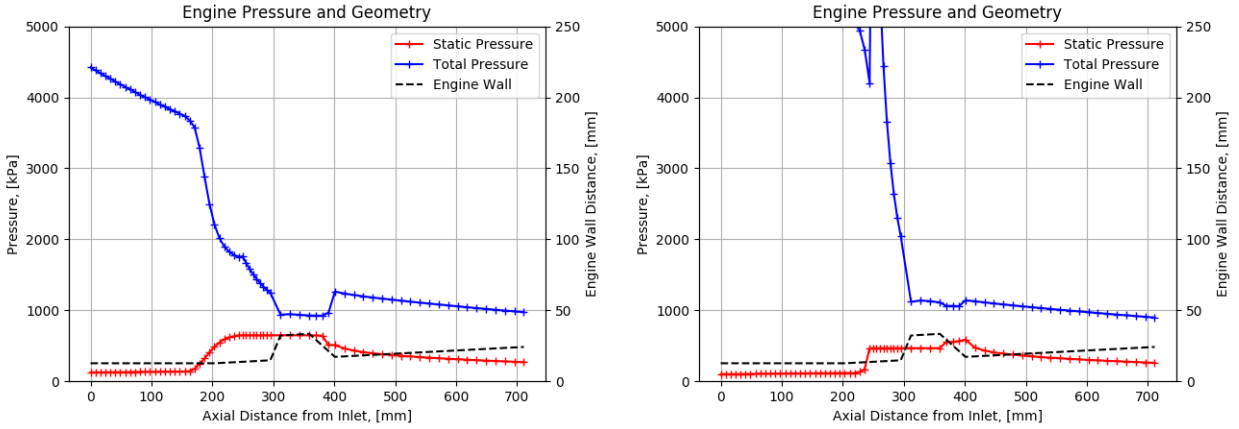

(a) Case 1 pressure values

(b) Case 2 pressure values

Figure 3.13: Static and total pressure values from CReSS evaluation of selected HIFiRE cases

As seen in Fig. 3.13, the total pressure has a spike in the same location as the total enthalpies in Fig 3.12. Additionally, it is seen that the jump occurs on the choke point of the combustor, hinting at integration difficulties near sonic velocities. At the same axial locations in the engine, a sudden change in Mach can be seen in Fig 3.10, further supporting the theory of integration issues near sonic velocities. It is also a possibility that the engine is choking before reaching the critical area, as the model currently does not have a method of adjusting upstream conditions for such an issue.

With the cavity issues addressed, it is also necessary to consider the combustion process and make sure it is operating as intended. Plotting the mass fractions for the major species(excluding N_2), Figs. 3.14 and 3.15 were created. For both cases, it is clearly seen that the majority of the combustion takes place as the mixture enters the cavity around x = 300 mm, however it was assumed that the mixture had minimal reactions until it entered the

cavity. Downstream of the cavity entrance, the mass fractions of the combustion products, CO_2 and H_2O, increase while O_2 decreases as expected. It can also be seen that the C_2H_4 - CH_4 fuel mixture is consumed rapidly, however due to the continuing downstream reactions of the other major species, it is likely that radicals from the air/fuel mixture are still present. Such behavior can was seen in the HIFiRE simulations documented in *Gruber, 2008*. To verify this speculation the CO, CH, and OH radicals, were added to figs. 3.14 and 3.14.

As shown by the mass fractions, the radicals do not exist before the sudden change in oxygen and fuel, and decrease with similar trends as the combustion products are produced. This supports the theory on the sharp decrease in fuel and oxygen as the flow enters the cavity. It should be noted that the mechanism used spans many more species than the few selected, however, a majority of those not shown have mass fractions near zero such that it was decided not worth plotting them. Additionally, two reaction mechanisms were compared and yielded similar results: One being an Ethelyne-air mechanism retrieved from the USC database [49], the other being the high temperature GRI-30 mechanism.

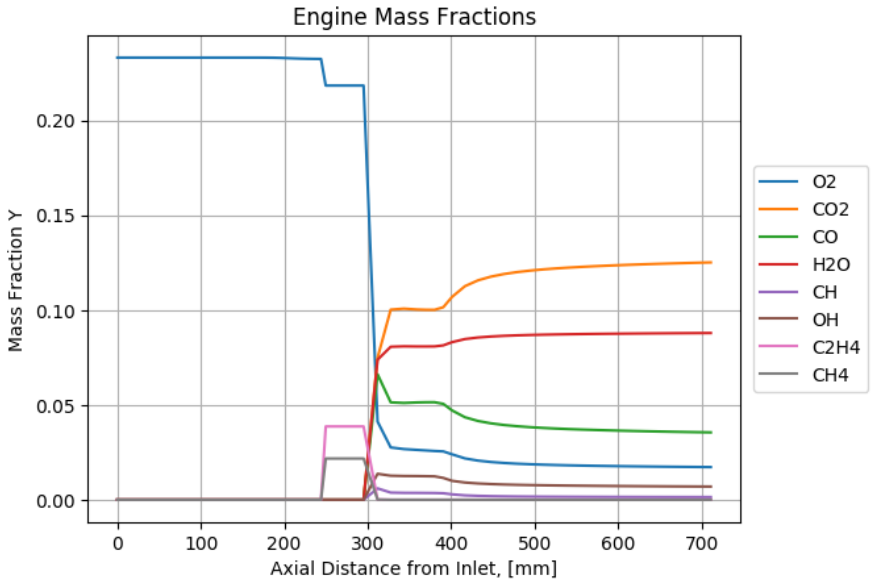

Figure 3.14: Mass fractions of major species as predicted by CReSS for Case 1 of the HIFiRE data

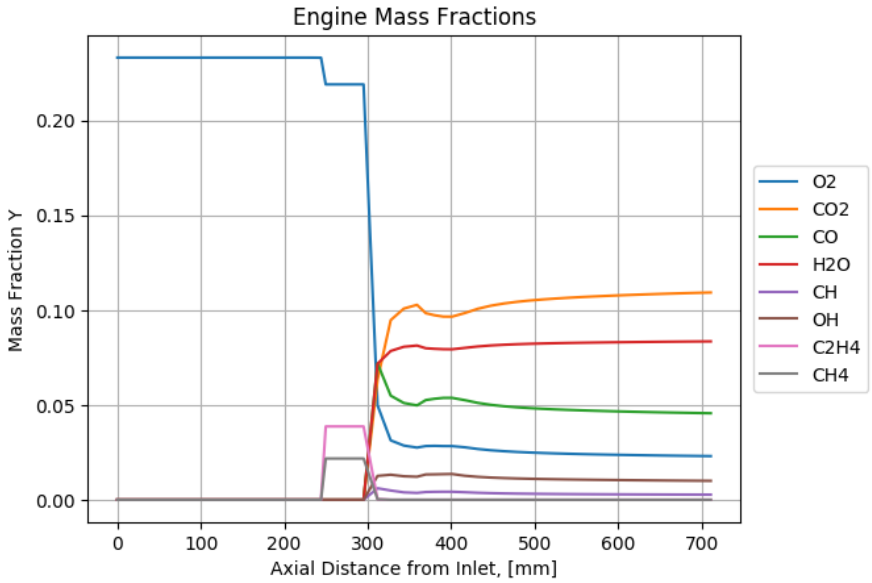

Figure 3.15: Mass fractions of major species as predicted by CReSS for Case 2 of the HIFiRE data

3.4 Engine Structural Analysis

To achieve the stated goal of optimizing an engine structure as well as the engine flow-path, a self-generating structural analysis must be used. This introduces many programming and logistic challenges however overcoming these is a first step towards capturing the fluid-thermal-structural interactions that are an area of interest to HVSI and other research programs. The engine geometry considered consists of axisymmetric cross-sections, which excludes the geometry from the HIFiRE cases. This restriction allows for this work to focus on the automation of structural analysis, and the expansion to planar symmetric engines are left to future work.

3.4.1 FEA Solver Selection

Simulating the thermal/structural interactions of an engine is commonly done using commercial software packages which use various Finite Element Methods (FEM). Such a simulation is often referred to as a Finite Element Analysis (FEA), and will be done to consider how the engine's structure behaves. Two of the more prominent FEA software packages are ANSYS and Abaqus, however these require licenses that are prohibitively expensive for some or have educational versions that are limited in model size. There are many open source programs as well, such as Elmer, FreeFEM++, and CalculiX, however each of these has its limitations.

With the goal of automating the analysis process, the selected software must have a scripting interface with the programming language of choice, which is Python. This was decided as the optimization package selected, Dakota, has a direct Python interface which increases communication between the optimization software and the simulation [50]. This

requirement complicates things as none of the software packages are written in Python, however the software FreeCAD is able to be imported to Python as a module and acts as an interface with some of the open source solvers, particularly Elmer and CalculiX. Utilizing FreeCAD also has the benefits of constructing a 3D model of the engine as well as interfacing with meshing packages such as Gmsh and Netgen. For this work Gmsh will be used.

The meshing algorithm selected within Gmsh is a frontal algorithm, selected for its stability in the varying geometries. Also called advancing front techniques, frontal algorithms use the external surfaces of a volume as boundary surfaces and constructs new elements one at a time using the existing nodes on the boundaries [51]. The specific frontal algorithm used by Gmsh is based on the work of J. Schoberl and is also used by Netgen [52].

Due to its ease of implementation, and the added benefit of solving the thermal fields and strain fields simultaneously, the CalculiX solver will be employed. The simultaneous solving of the fields is beneficial to this study as it allows for better simulation of the thermal/structural interactions, a primary goal of this paper. This sets CalculiX apart from other packages like ANSYS, which solves the thermal and stress fields separately.

3.4.2 Geometry Construction

The first step in completing the FEA is creating a geometry to mesh, which requires a set of points defining the axisymmetric cross-section. Once material thickness values are assigned to each point, this can easily be extrapolated from the flow-path geometry. An example of this geometry process can be seen in Fig. 3.16 which is then used to create a FEM mesh using Gmsh [52], which can be seen in Fig. 3.17. To accurately define a FEM mesh, it is a collection of simple geometric shapes such as tetrahedrons, prisms, and pyramids

that make up a larger defined shape or volume [52].

The process of generating the 3D mesh from the flow-path diameters requires a few inputs, the most important of which is the characteristic length which dictates the resolution of the mesh. For this work, it is critical to balance the resolution of the mesh with the volume of the engine as the structural analysis will be run at every iteration of the optimizer. In the case at which the resolution is too high, the computational time of each individual analysis increases rapidly and even more so for the optimization process, however if the resolution is too low, critical thermal/structural phenomena will not be captured. Capturing these phenomena with increased resolution is made possible through use of high powered computing, one of the primary approaches of HVSI [21].

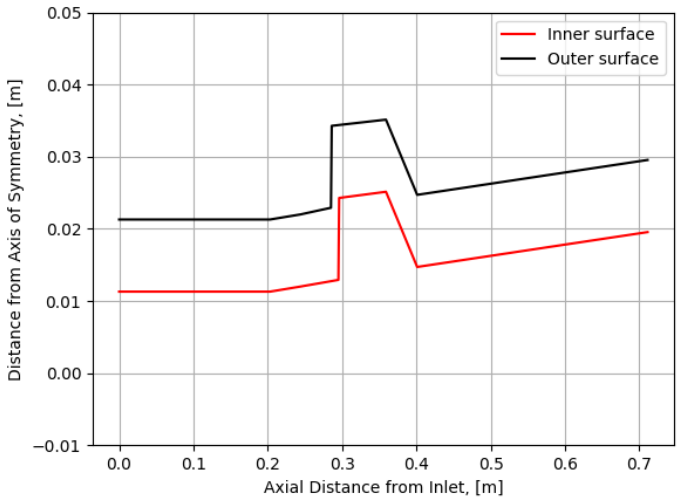

Figure 3.16: Engine structure cross-section generated from flow-path geometry

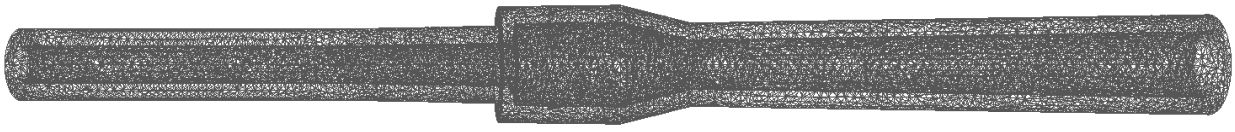

Figure 3.17: Example 3D mesh generated from the geometry shown in Fig. 3.16

Due to the algorithms used by Gmsh, the mesh created is ”unstructured” which means that ”the elements are completely defined simply by an ordered list of their nodes” with no predefined ordering relation between nodes [52]. While this suits the needs of this work, the computational time would be significantly reduced if a structured mesh were introduced. Switching to a structured mesh should be considered for future work.

After refinement, it was decided that a maximum characteristic length of 15 mm was sufficient to maintain accuracy without excessive computational times. This length was selected after a mesh case study considering the displacements, which found that a characteristic length of 10 mm was sufficient to prevent asymmetric deformation in the radial direction. This condition was selected as a axi-symmetric design with one-dimensional internal flow should have axi-symmetric deformations and stresses.

3.4.3 Boundary Conditions and Applied Loads

In structural analyses, the method of which the loads are applied are almost as important as how the loads are calculated and are entirely dependent on what is being simulated. In this work, the engine being simulated is assumed to be set up in a direct-connect test setup which is briefly described in Sec. 1.3.

The structural boundary conditions used for this test is a fixed face on the upstream end at station 2, and fixing the downstream end (station 4) in the axial direction only. Restricting only the displacement in the axial direction is critical as it allows the combustor/nozzle to expand and contract radially, or breathe. While it would be ideal to apply the same boundary condition to station 2, doing so would allow for rigid body motion in the radial direction. Due to the higher temperatures and combustion products, it was

decided that the downstream end will be allowed to breathe and the upstream end will be fixed. Expansion of the engine components is expected due to a combination of the pressure loading as well as the high thermal loads.

For the remaining boundary conditions, it is convenient to divide the engine surfaces up into two groups, internal and external. The internal surfaces consist of the flow path boundaries while the external surfaces, in a ground test, face the facility environment. Despite the less hazardous conditions, it is necessary to define a heat transfer coefficient and pressure magnitude which acts on the external surfaces. The values used for this can be found in Table 3.2 whose temperature and pressure values are taken from the standard atmosphere model [32] and the film coefficient from *Long* [53].

Table 3.2: Ambient air values used for external surface boundary conditions

Property	Value
$p_{ambient}$	101325 Pa
$T_{ambient}$	300 K
$\boldsymbol{h}_{ambient}$	5 $\frac{W}{m^2K}$

The internal surface boundary conditions are generated from the flow-path simulation described earlier in this chapter with an added calculation for the heat transfer coefficient. Considering *Newton's Law of Cooling*

$$q_w = h_{conv}(T_w - T_e) \tag{3.32}$$

where q_w is the wall heat flux rate and the subscripts w and e denote the wall and boundary layer edge respectively, a heat transfer coefficient h_{conv} is defined [35]. For compressible flows, Eq. 3.32 is modified to yield an "effective" heat transfer coefficient

$$h_{conv_e} = q_w/(T_w - T_{aw}) \tag{3.33}$$

where T_{aw} represents the adiabatic wall temperature, or the wall temperature at which no heat transfer would occur [35, 54, 55]. The adiabatic wall temperature is calculated using a recovery factor as defined by the equation

$$T_{aw} = T_e + r\frac{u_e^2}{2c_p} \tag{3.34}$$

with the recovery factor r estimated using $r = \sqrt{Pr}$ for laminar flows and $r = \sqrt[3]{Pr}$ for turbulent flows [35, 54, 55]. For this analysis, the flow will be assumed to be turbulent throughout the engine.

It is useful to define a non-dimensional heat transfer coefficient, the *Stanton Number*, as

$$St = \frac{h_{conv}}{\rho u_e c_p} = \frac{Nu}{RePr} \tag{3.35}$$

where Nu is the *Nusselt Number* determined by the *Colburn equation*

$$Nu = 0.023 Re^{0.8} Pr^{1/3} \tag{3.36}$$

taken from *Rouse and Sleicher* [56]. While this does complete the system, there are more accurate methods for determining the heat transfer coefficient for high speed flow such as the *reference temperature method* developed by Eckert [35].

This method describes a reference state defined by a reference temperature T^* calculated using

$$T^* = T_e + 0.5(T_w - T_e) + 0.22(T_{aw} - Te) \tag{3.37}$$

which is assumed to be an average of temperatures across the thickness of the boundary layer [57]. It is assumed in this work that $T_w = T_{aw}$ for this estimation which decreases the

accuracy of the calculation by increasing the calculated heat transfer coefficient, however, the inaccuracy is deemed acceptable as the flow simulation is assumed adiabatic. A reference Stanton number defined by

$$St^* = 0.332(Pr^*)^{-2/3}(Re^*)^{-1/2} \tag{3.38}$$

is then calculated where the superscript * denotes values calculated at the reference state [35]. The reference state is determined using the reference temperature from Eq. 3.37 along with the pressure and mass fractions from the flow path simulation. The use of Eqns. 3.34, 3.35 and 3.38 allows for the effective heat transfer coefficient h_{conv_e} and adiabatic wall temperature T_{aw} to be calculated at every axial location in the engine, completing the thermal boundary conditions needed for the engine's internal surfaces.

Unlike the thermal boundary conditions, the pressure acting on the internal surfaces come directly from the flow path simulation and need no additional calculations. Since it is assumed that the flow is one dimensional, the pressures can be defined as $p = p(x)$ where the pressure acts normal to each face. Similarly, the adiabatic wall temperature and heat transfer coefficients can be represented as $T_{aw} = T_{aw}(x)$ and $h_{conv_e} = h_{conv_e}(x)$, respectively. For each element face that the flow-path environment acts upon, the x-coordinate is that of the faces' centroid determined from the elements' nodes. Additionally, it is assumed that the pressure, temperature, and heat transfer coefficient distributions are uniform across the face of each element.

To show an example of the code running, a sample case was created using similar conditions as the HIFiRE Case 2 but with axisymmetric geometry, which can be seen in the mesh in Fig. 3.17. The internal loads applied to such a mesh can be seen in Fig. 3.18, which shows the adiabatic wall temperature, heat transfer coefficient, and pressure distributions

along the axial direction. These boundary conditions were then applied to a mesh and a 5

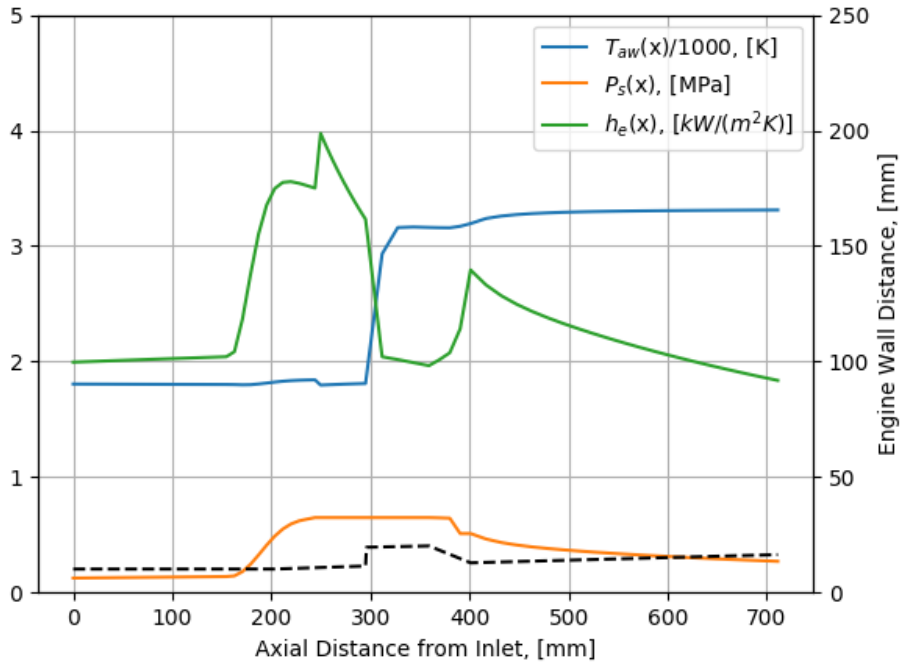

Figure 3.18: Sample boundary conditions applied to engine geometry

second transient study was ran. Mapping the temperature results back onto the mesh yield Fig. 3.19, in which the different parts of the flow path can be seen to experience different heating conditions.

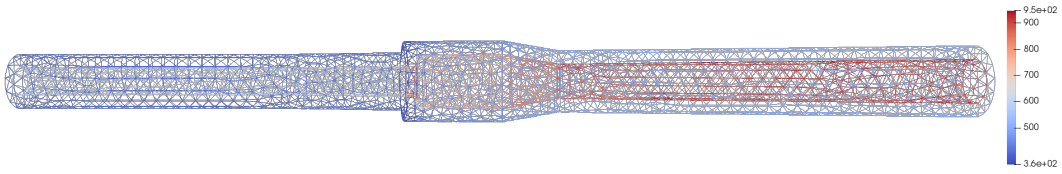

Figure 3.19: Engine mesh with temperature results overlay after 5 seconds of simulated run time

In addition to mesh overlays, the stress, strain and displacement values can be post-processed to retrieve max/min values as well as plot contours similar to that of Fig.

3.20. The stress, strain, displacement values are all computed and will be used as boundary

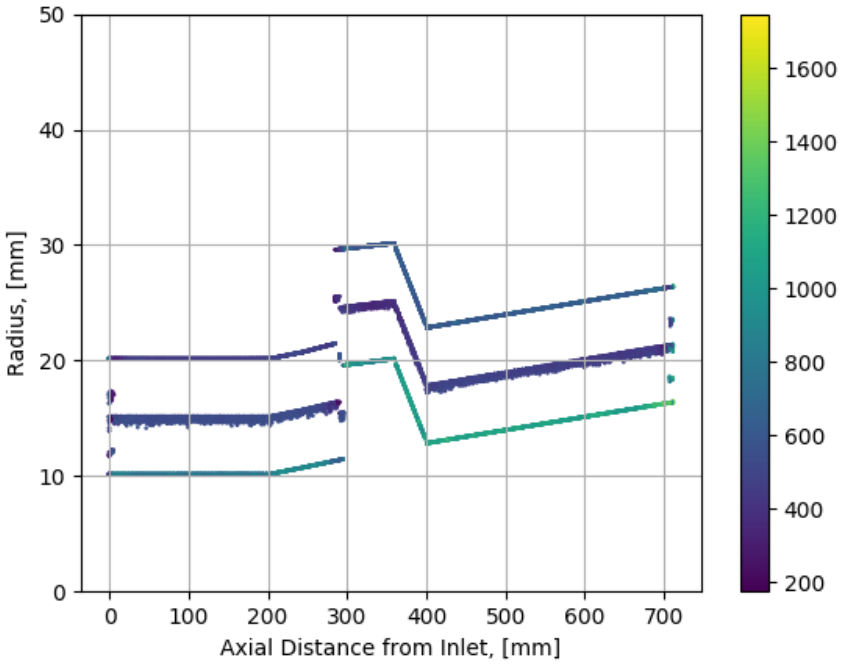

Figure 3.20: Stress contour in MPa plotted over a cross-section reduced from 3D mesh to 2D cross-section

constraint values in the optimization section. Additionally, the engine mass can be calculated and minimized to create a lighter weight engine.

Considering the operation of the engine, it was found through a short study that for a structure without a cooling method, the run time must be kept relatively low, typically around 5 seconds. This finding will be used for the optimization described in the following chapter. This concludes formulating the automated structural analysis.

Chapter 4

Optimization of System Components

This chapter discusses the use of the previous analysis methods to optimize a ramjet or scramjet design for steady state operation. With the various numerical methods used, there is a level of uncertainty in the results which carries over to the gradients calculated in an optimization algorithm. These uncertainties then cause the design space gradient to seem more or less steep than it is, resulting in either an increased convergence time or cause a convergent function to diverge. For these reasons the numerical uncertainties must be taken into account when selecting the optimization algorithm, constraints, objective functions, and the convergence tolerance.

4.1 Objective Function Selection

Due to the variety of vehicles on which scramjets may fly and the various design decisions involved, the optimal performance parameter differs for each engine design. The common parameters for minimizing or maximizing are the system thrust, efficiency, and mass, where efficiency can be quantified using either thrust specific fuel consumption or specific impulse. With the simulation discussed in Ch. 3, these parameters are relatively simple to calculate from the resulting data. In this work, the thrust is determined through treating the entire engine as a control volume and applying the conservation of momentum

in Eq. 2.4. Assuming all thrust $\boldsymbol{T}$ acts in the x-direction, Eq. 2.4 becomes

$$\sum F_x = \int_{cs} u\rho(u \cdot n)dA \tag{4.1}$$

For subsonic exhaust, the exhaust pressure is equal to the ambient pressure and the relation $\sum F_x = \boldsymbol{T}$ applies. This does not necessarily hold true for supersonic exhaust plumes that are seen in ramjets and scramjets, thus the equation

$$\sum F_x = (p_a - p_e)A_e + \boldsymbol{T} \tag{4.2}$$

is used where the subscripts represent the ambient and exhaust flows, respectively [9].

Combining Eqs. 4.1 and 4.2 and evaluating the integral term results in the final thrust equation

$$\boldsymbol{T} = \dot{m}_e u_e - \dot{m}_a u_a + (p_e - p_a)Ae \tag{4.3}$$

For systems that do not exhaust to a chamber, this work assumes that subscripts a and e represent the furthest upstream and downstream locations, respectively.

Related to thrust is the thrust specific fuel consumption c_t which is used as a measure for how much fuel is consumed per unit of thrust. This parameter is of interest as it greatly influences the the range of an aircraft, as seen in the *Breguet Range equation*

$$Ra = \frac{u_\infty}{c_t}\frac{L}{D}\ln\frac{W_0}{W_1} \tag{4.4}$$

which uses c_t, dry/wet weight ratio, and the lift-to-drag ratio to estimate an aircraft's range Ra [58]. Since the work here is limited to the propulsion system, minimizing c_t is considered

instead of maximizing range, where c_t is calculated using the following equation.

$$c_t = \frac{\dot{m}_f}{\boldsymbol{T}} \tag{4.5}$$

This is necessary to consider as increasing the range of high speed craft has been of interest since the scramjet was conceived [3]. Another and more widely used efficiency metric is the specific impulse defined by

$$I_{sp} = \frac{\boldsymbol{T}}{\dot{m}_f g} \tag{4.6}$$

where g is the acceleration of gravity assumed to be $9.81 m/s^2$ [9].

As discussed in Sec. 1.2, the I_{sp} of ramjets and scramjets is higher than rockets operating at similar speeds other propulsion systems cannot reach, as shown by Fig. 1.5. Due to this dependency, it is of interest to maximize the I_{sp} through increasing the thrust and decreasing the fuel mass flow rate. In contrast to the previous parameters of vehicle performance, the final parameter of interest is the mass of the engine based on the structure volume V_{struct} and material density ρ_{struct}.

$$m_{engine} = \rho_{struct} V_{struct} \tag{4.7}$$

As with other aircraft components, it is desirable to minimize the mass of the engine, especially if it is to be flight hardware. Similarly, minimizing cost is a large focus for optimization efforts, but with its heavy dependence on fabrication methods it will not be considered here.

With the parameters defined, it is necessary to select which performance parameters are of importance for each design. The relationship between the different parameters should also be considered, most notably that c_t and I_{sp} approach more desirable values as thrust increases. Indirectly, the engine mass is related to the 1-D simulation through the thermal

and pressure loading acting on the walls, and is constrained by the material properties of the structure. This completes the description of the objective functions relevant to this work, however a final note must be made that the values of the performance parameters may not seem consistent with other engines due to the lack of inlet and expansion component models.

4.2 Constraint Selection

The optimization performed here is subjected to various constraints from the vehicle size, performance requirements, and limitations of the simulation. Constraints due to the vehicle size are self explanatory, as the propulsion system must fit within the airframe otherwise it may interfere with other systems. A singular performance constraint is of interest here, and it is that the shock train length does not exceed the length of the isolator. This is done such that operation of the system inlet, which is not considered in this work, is not affected by the shock train and thus is not at risk of an un-start, as discussed in Sec. 3.1.1. The constraint on the shock train can be described by an inequality function

$$g(\mathbf{x}) = L_{iso} - L_{st} \leq 0 \tag{4.8}$$

where L_{iso} and L_{st} are the lengths of the isolator and shock train, respectively.

The function $g(\mathbf{x})$ will be used to define the following constraints as it is common nomenclature for describing inequality constraints in optimization problems where $\mathbf{x}$ is a vector of input variables [59]. Another flow-path constraint is made to enforce supersonic exhaust from the combustor. This behavior is represented by the inequality

$$g(\mathbf{x}) = 1 - M_4 \leq 0 \tag{4.9}$$

where M_4 is the Mach number at station 4.

The limitations of the simulation are important to consider when applying constraints, as the optimizer may find an "optimum" that the simulation is not modeling correctly. This necessitates that the geometry and inlet conditions must be similar to that of the validation cases. Additionally, it is necessary to have a coarse convergence rate as the FEA mesh is not refined to keep computational time within reasonable bounds.

In addition to the constraints from the flow simulation, the structural analysis imposes its own constraints to ensure structural integrity. The first constraint of importance is a limit on Von Mises stress, which must be kept below the yield stress of the selected material. This constraint is implemented by finding the maximum Von Mises stress of the FEA and enforcing the constraint

$$g(\mathbf{x}) = \max(\sigma_{FEA}) - \sigma_y \leq 0 \tag{4.10}$$

where σ_{FEA} is the nodal Von Mises stress results of the FEA and σ_y is the material yield stress. Similarly, the temperature of the material must stay below the materials elastic limit. This can be represented by the inequality constraint

$$g(\mathbf{x}) = \max(T_{FEA}) - T_{Limit} \leq 0 \tag{4.11}$$

where T_{Limit} represents the temperature at which the material no longer exhibits elastic behavior.

It was previously mentioned that geometric constraints must be put in place to keep the flow-path simulation near the cases with which it was validated. To do this, a series of constraints were made to enforce a converging or straight isolator, a diverging mixing

zone, a positive cavity depth, and enforcing that the nozzle throat is the geometric critical area. These are enforced by the inequalities

$$g(\mathbf{x}) = D_3 - D_2 \leq 0 \tag{4.12}$$

$$g(\mathbf{x}) = D_3 - D_{3.1} \leq 0 \tag{4.13}$$

$$g(\mathbf{x}) = -L/D \leq 0 \tag{4.14}$$

$$g(\mathbf{x}) = D_{3.5} - (D_{3.1} + 2L_{cav_t}/(L/D)) \leq 0 \tag{4.15}$$

$$g(\mathbf{x}) = D_{3.5} - D_4 \leq 0 \tag{4.16}$$

which are evaluated at each step of the optimization and the results are returned to the optimization algorithm. This completes the definition of constraints which will be used, not including the bounds found in a later study.

4.3 Algorithm Selection

The selection of optimization algorithms is heavily dependent on the objective function and constraint formulation. More specifically, it is dependent on the availability of gradients and hessians, which provide information on the contours of both constraints and objective functions. In the case of the simulation formulated in Ch. 3, the gradients and hessians are not able to be calculated directly. Due to the increased computational time of the FEA, the gradients are not able to be calculated efficiently, giving preference to gradient-free methods such as direct search and evolutionary methods.

Dakota provides access to a variety of gradient-free optimization methods, those

of interest being the asynchronous pattern search, mesh adaptive direct search, and genetic algorithms [60]. Due to the high computational requirements of the structural analysis and the typically high numbers of iterations needed by genetic algorithms [59], it was decided to exclude genetic algorithms leaving the remaining pattern search methods. Due to the nature of the asynchronous pattern search algorithm in Dakota, it is most useful when parallel computing is available. With the limited computational resources available, it was decided to run the optimization as a serial process, thus the mesh adaptive direct search algorithm was selected.

4.4 Railgun Launched Scramjet Optimization

Considering the case of a railgun launched scramjet powered vehicle, it is important to identify the propulsion performance parameters which would most benefit the performance of the vehicle. In this scenario, the vehicle's performance benefits from having a propulsion system which maximizes the speed and acceleration, both of which benefit from higher thrust and lower system mass. As a result, the thrust and engine mass are considered to be the objective functions. The starting design for this optimization is as described in Table 4.1, where the variables defined can be represented in Fig. 4.1. It should be noted that the L/D in this case is not the lift-to-drag ratio of an aircraft, but rather the cavity length to depth ratio as shown in Fig. 3.7.

Two preliminary studies were performed using the flow-path simulation to map the thrust contour in regards to pairs of the design variables to obtain a better understanding of the design space. The first of the studies was performed by freezing all variables except for equivalence ratio ϕ and the cavity L/D ratio. This method produced the contour seen

Table 4.1: Starting design point for optimization of a scramjet engine

Variable	Value	Units
ϕ	0.9	n/a
L_{iso}	250	mm
L_{mix}	50	mm
L_{cav_t}	100	mm
L_{cav_r}	40	mm
L_{comb}	300	mm
D_2	40	mm
D_3	38	mm
$D_{3.1}$	41	mm
$(L/D)_{cav}$	14	n/a
$D_{3.5}$	45	mm
D_4	70	mm
t	30	mm

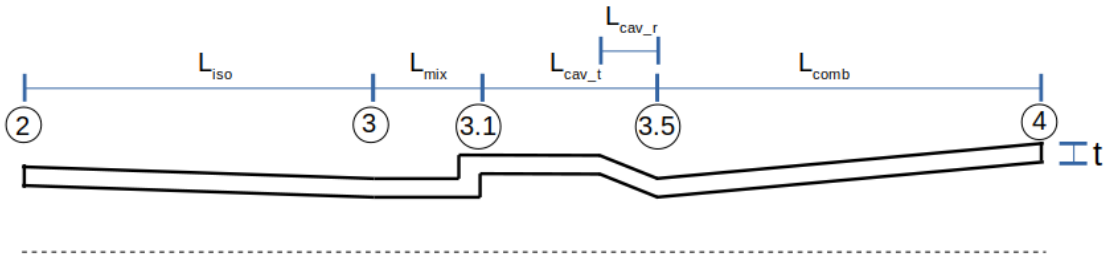

Figure 4.1: Conceptual scramjet design with relevant variables for optimization

in Fig. 4.2 where it is seen that the engine loses all thrust at high L/D ratios as well as low ϕ values. The decreasing thrust with decreasing ϕ is expected as ϕ dictates the fuel mass flow rate, however the sudden drop due to increasing L/D is not expected. It is thought that the prescribed separation region is no longer valid with high L/D ratios, and thus it will be bounded between 7 and 14. This emphasizes the need for a more accurate method of simulating the re-circulation zones present in the cavity flameholder, however the implemented model is sufficient for this work.

The second study performed considered the relationship between the equivalence ratio and the throat diameter, $D_{3.5}$, which yielded the contour in Fig. 4.3. Considering this

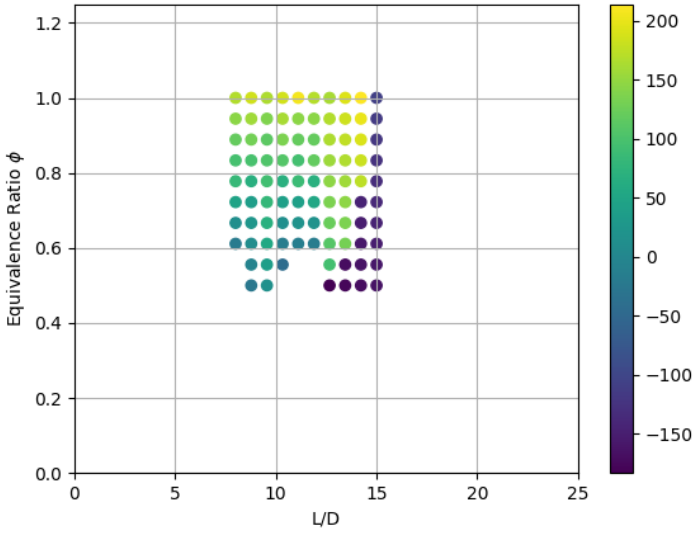

Figure 4.2: Simulated thrust contour, Newtons, in relation to fuel equivalence ratio and cavity geometry L/D

contour, it can be shown that the thrust increases with a smaller throat diameter, however, recalling the discussion in Sec. 3.3, it must be considered that a reduced throat diameter may lead to artificially inflated thrust values. An interesting behavior displayed in Fig. 4.3 is the thrust values as $D_{3.5}$ increases and some insight may be drawn. Such an insight may be that when the thrust is at its minimum, the throat is relatively the same diameter D_4 resulting in no expansion of the flow before passing through station 4.

It is shown in both Figs. 4.2 and 4.3 that there are some points missing from the sweep, particularly at lower ϕ values. This is because the points with subsonic exhaust were removed as the thrust values heavily skewed the contour ratio and the constraint described in Eq. 4.9 must be applied. With these contours in consideration, it is now possible to move forward with an optimization of the flow path and the engine structure. For this optimization, the material properties of Incoloy 909 were used, as was recommended in *Heiser and Pratt*, and are tabulated in Table 4.2.

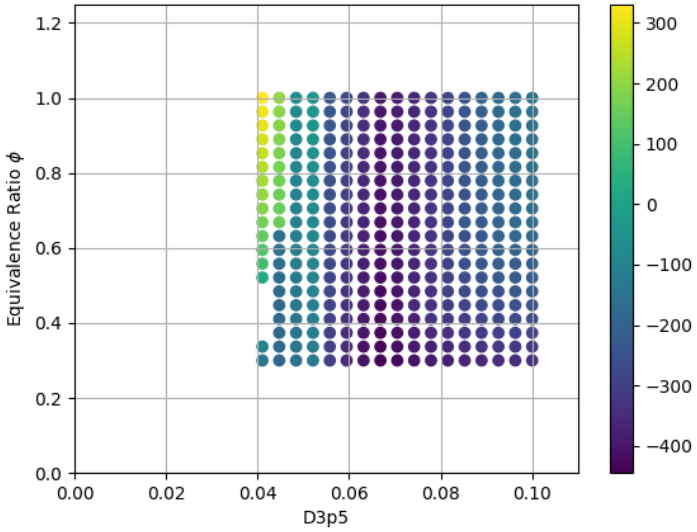

Figure 4.3: Simulated thrust contour, Newtons, in relation to fuel equivalence ratio and throat diameter in meters

Table 4.2: Relevant material properties of Incoloy 909 [1, 15]

Property	Value	Units
E	159	GPa
ν	0.3	n/a
ρ	8190	kg/m^3
k	22.5	$W/(m.K)$
c	600	$J/(kg.K)$
α	$9.18 * 10^{-6}$	$1/K$
σ_y	950	MPa
T_{Limit}	950	K

To keep the model within environments similar to the validation cases, the optimized case will use the same inlet conditions as Case 2 from Table 3.1 as well as the external

boundary conditions described in Table 3.2.

After many evaluations spanning roughly 10 hours, the optimizer found the "most feasible" design, described in 4.3. This design is infeasible as it violates the yield stress

Table 4.3: "Most feasible" design point for optimization of a scramjet engine

Variable	Value	Units
ϕ	1	n/a
L_{iso}	250	mm
L_{mix}	200	mm
L_{cav_t}	100	mm
L_{cav_r}	50	mm
L_{comb}	300	mm
D_2	40	mm
D_3	30	mm
$D_{3.1}$	50	mm
$(L/D)_{cav}$	14	n/a
$D_{3.5}$	45	mm
D_4	60	mm
t	30	mm

constraint, maximum temperature constraints, and the shock train constraint. With that said, the shock train constraint can be resolved by extending L_{iso} by 50 mm. Similarly, the yield strength violation can be reduced by decreasing the wall thickness to 20 mm, and the temperature constraint violation can be reduced somewhat by decreasing ϕ to 0.8. The temperature results of this modified design can be seen in Fig. 4.4 where it can be seen that

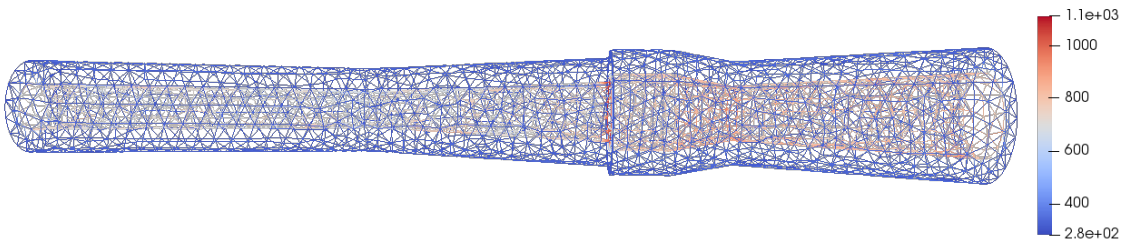

Figure 4.4: Modified optimization result temperature(K) contour

the highest temperature occurs at the upstream part of the cavity. This is a result of there being a corner with two faces being heated at that point, thus more heat being transferred into that portion of the structure. Aside from that hot-spot, all of the other nodes seem to be well below T_{Limit}.

Despite Dakota not finding a feasible optimum, the optimization process yielded a lot of information on the coupled analyses and their respective limitations. From what was learned here, it can be said the coupled simulation works as intended, however, the structural design being considered needs a more suitable material or a method of reducing the heat loading on the engine structure to simulate longer run times.

Chapter 5

Closing remarks

5.1 Conclusions

A quasi-1D ramjet/scramjet simulation, CReSS, was formulated and compared with Vulcan CFD results for two different cases. The simulation built utilized a combination of physics based-models and experimental correlations, while modelling the combustion using chemical kinetics in the form of canonical reactors. Provided with the initial conditions and fuel equivalence ratio, CReSS showed good agreement with the validation cases, however, an increase in total temperature and total pressure were seen near the sonic point of the flow indicating the flow is choking before the critical area which is not possible. A possible solution was suggested and recommended for future use. Despite these discrepancies, it was shown that CReSS can simulate the transition from subsonic to supersonic flow which occurs in dual-mode scramjets.

CReSS uses a simple Fanno flow model for the isolator section upstream of the shock train, and uses an experimental correlation provided by *Waltrup and Billig* to estimate the shock train length based on the pressures at either end of the isolator. The pressure of the combustor is estimated using a method described in *Heiser and Pratt*, which uses a shock-free isolator and combustor solution to determine the pressure at the entrance of the combustor. Modelling the flow within the shock train is done using the psuedo-shock method described

by *Weiss and Grzona* which shows good agreement with the validation cases.

The formulation of CReSS' combustor simulation involved the derivation of modified plug flow reactors. Standard plug flow reactors, described by *Turns*, assume frictionless walls and steady-state, and integrate a set of ordinary differential equations across the one dimensional domain. The newly derived reactors no longer assume frictionless walls, which allows for more accurate simulation of high-speed reacting flows in a 1D model. In addition, a constant pressure plug flow reactor was derived for the combustor analysis method described in *Heiser and Pratt* where the pressure is assumed to be constant across the combustor. Comparison with HIFiRE data showed that this assumption is not the best in higher speed cases.

It was found that the use of a prescribed separation zone in cavity-based flameholders does hurt the robustness of CReSS, as does the lack of a mixing model. Introducing new models for these issues would greatly benefit CReSS in range of usability and model accuracy. CReSS was also implemented with an oblique shock wave that forms on the downstream end of the cavity similar to that shown by the work of *Ben-Yakar and Hanson*. The solution was found through iterating the wave angle and matching the enthalpy and mass flow rate on the upstream and downstream sides. Implementing this model increased the model accuracy significantly for the cases with supersonic flow in the cavity flameholder.

CReSS was paired with a self-generating finite element analysis to model a short transient period and the resulting stress on the engine structure. The finite element analysis performed utilized an unstructured axi-symmetric 3D mesh, however the solver, CalculiX, is not limited to axisymmetric geometries. It was found that without a cooling solution, the transient period must be kept on the order of seconds. The coupled analyses were then used to optimize a conceptual scramjet design, considering flow path geometry, structural com-

ponents, and fuel equivalency ratio as design variables. This optimization was constrained to maintain the structural integrity through limiting the maximum stress and metal temperature values.

For the optimization case selected, the optimum solution would have high thrust and low weight, thus the objective functions selected were the thrust and mass of the engine. After many iterations, the optimizer provided not a feasible engine design, but a most feasible design. This engine design can be modified to nearly satisfy the constraints, however if CReSS were given some improvements to increase stability and fidelity, the optimizer would likely find a feasible optimum given enough time and an adequate convergence tolerance.

The development of CReSS was performed with the goal of predicting the properties of the flow through the engine, simulate the combustion processes, and to estimate the performance characteristics of a scramjet engine. This was demonstrated with the comparison to the HIFiRE simulations available, and then again in an optimization setting. Along with CReSS, a self-generating thermal-structural finite element analysis was developed to consider the effects the flow path has on the engine structure. These coupled analyses were then used in a conceptual design optimization to demonstrate the capabilities of CReSS as well as highlight some areas where improvements can be made.

The developed analysis system allows for rapid determination of performance and feasibility of conceptual designs. CReSS simulates the flow path from which performance parameters may be derived, allowing for parametric studies to be done with a wide set of design variables. The self-generating finite element analysis extends the simulation to thermal/structural interactions and consider the feasibility of the design. Coupling the two analyses allows for automated exploration of the design space as well as optimization of preliminary designs as shown by this work.

5.2 Future Work

While the work described here is capable of simulating high-speed propulsion systems with a degree of accuracy, it is important to reiterate that the model formulated is a first step towards other topics of interest and simulation capabilities. These topics are focused on high speed propulsion systems but can be extended to include other systems of high speed vehicles.

5.2.1 CReSS Improvements

As discussed in Sec. 3.3, the simulation code described has limitations that are a result of assumptions made during formulation, namely the prescribed re-circulation region in the cavity. This assumption, and the resulting issues with total enthalpy and total pressure in the near-sonic regime, allow for significant improvements in the CReSS formulation. A possible solution would be to utilize a numerical shooting method to enforce the correct Mach number at the throat by changing the combustor pressure or by changing the re-circulation zones' profile.

One aspect that the current CReSS formulation omits is a mixing model, which would greatly improve the robustness of the simulation. Similarly, the current model also omits the re-circulation of products back into the core flow occurring in the cavity. This re-circulation is a key aspect of cavity-based flame-holders and is necessary to better simulate such a geometry. While there are other improvements that could be made, these are seen as the most prominent ones.

5.2.2 Thermal Management Design Study

Shown by the short run time of the structural simulations in Ch. 4, a major challenge in designing high speed engines is the management of thermal loads. There are a plethora of methods used, the more prominent design being regenerative cooling discussed in Sec. 2.3. A possible use for CReSS is to determine flow path loading for which a regenerative cooling system can be designed or optimized. Another topic of possible research is the use of thermal barrier coatings, which is the use of a ceramic coating to protect engine components from high heat loads and thus extending the operational time of a propulsion system.

5.2.3 Hypersonic Vehicle Studies

One of the goals mentioned earlier was to develop a model that can be used in a full vehicle simulation to determine vehicle wide performance parameters and optimized on a vehicle system scale. The model developed here, while it does not include an inlet or external nozzle model, can easily be expanded to include those to assist in airframe-engine integration. Additionally, due to the relatively short computational time of CReSS, it can be used in an iterative manner for vehicle-wide optimization or trajectory optimization.

5.2.4 Incorporation of 3D Computational Codes

While improvements to CReSS can be made to increase its accuracy, it is a 1D model and thus will not capture some phenomena of interest. These phenomena include the re-circulation occurring in the cavity, fuel injection, and shock-waves that may form in the cavity. While there are experimental correlations that attempt to model the behavior,

the correlations have their own set of limitations that fall apart when different geometries are being considered. Incorporating 3D computational models add significant capabilities, namely the ability to model geometries that have fewer than 2-planes of symmetry.

5.2.5 Inlet Distortion Generation for Direct-Connect Tests

Due to the high cost of flight tests, there is significant effort in developing methods to simulate inlet distortions during a ground test for ramjets [28]. Similar efforts are ongoing at Virginia Tech for turbofan inlet distortion, as well as the use of plasma actuators in supersonic flow. Improved high speed simulation capabilities would benefit these efforts as well as benefit follow-on propulsion system simulations.

Bibliography

[1] William H. Heiser, D. T. P., *Hypersonic Airbreathing Propulsion*, American Institute of Aeronautics and Astronautics, 370 L'Efant Promenade, SW, Washington, DC, 20024-2518, 1994.

[2] Aviastar, "Leduc 010," , 1953. URL http://www.aviastar.org/air/france/leduc_010.php.

[3] Paul J. Waltrup, F. Z., Michael E. White, "History of Ramjet and Scramjet Propulsion Development for U.S. Navy Missiles," *John Hopkins APL Technical Digest*, Vol. 18, 1997.

[4] Joseph M. Hank, R. C. M., James S. Murphy, "The X-51A Scramjet Engine Flight Demonstration Program," *International Space Planes and Hypersonic Systems and Technologies Conference*, AIAA, 2008.

[5] Falempin, F., "Ramjet and Dual Mode Operation," *Advances on Propulsion Technology for High-Speed Aircraft*, Vol. 7, 2008, pp. 1–36.

[6] Shapiro, A. H., *The Dynamics and Thermodynamics of Compressible Fluid Flow*, John Wiley & Sons, Inc, 1953.

[7] "Schlieren Supersonic Shock Waves Image Gallery," , 2017. URL https://www.nasa.gov/centers/armstrong/multimedia/imagegallery/Schlieren/index.html.

[8] Anderson, J. D., *Modern Compressible Flow with Historical Perspective, 3rd Edition*, McGraw Hill, 1221 Avenue of the Americas, New York, NY, 10020, 2003.

[9] Philip Hill, C. P., *Mechanics and Thermodynamics of Propulsion, 2nd Edition*, Addison-Wesley Publishing Company, 1992.

[10] Turns, S. R., *An Introduction to Combustion: Concepts and Applications, 2nd Edition*, McGraw Hill, 1221 Avenue of the Americas, New York, NY, 10020, 2000.

[11] Smart, M. K., "Scramjet Inlets," Tech. Rep. 185-9, NATO, 2010.

[12] Mark R. Gruber, K. J., "Hydrocarbon-Fueled Scramjet Combustor Flowpath Development for Mach 6-8 HIFiRE Flight Experiments," Tech. Rep. 2010-2243, Air Force Research Laboratory, 2008.

[13] Smart, M. K., "Scramjet Isolators," Tech. Rep. 185-10, NATO, 2010.

[14] Adela Ben-Yakar, R. K. H., "Cavity Flame-Holders for Ignition and Flame Stabilization in Scramjets: An Overview," *Journal of Propulsion and Power*, Vol. 17, No. 4, 2001, pp. 869–877. doi:10.2514/2.5818.

[15] "Incoloy alloy 909," , 2004. URL http://www.specialmetals.com/assets/smc/documents/alloys/incoloy/incoloy-alloy-909.pdf.

[16] R. L. Chase, M. H. T., "A History of the NASP Program from the Formation of the Joint Program Office to the Termination of the HySTP Scramjet Performance Demonstration Program," *AIAA International Aerospace Planes and Hypersonics Technologies Conference*, Vol. 6, No. 95-6031, 1995.

[17] Peebles, C., "Learning from Experience: Case Studies of the Hyper-X Project," *47th AIAA Aerospace Sciences Meeting*, 2009.

[18] Lewis, M. J., "Global Strike Hypersonic Weapons," *AIP conference Proceedings*, Vol. 7, 2017.

[19] Christopher M. Rondeau, T. R. J., "X-51A Scramjet Demonstrator Program: Waverider Ground and Flight Test," *SFTE 44th International / SETP Southwest Flight Test Simposium*, 2013.

[20] Duo Zhang, Y. F., "Quasi-One-DimensionalModel of Scramjet Combustor Coupled with Regenerative Cooling," *Journal of Propulsion and Power*, Vol. 32, No. 3, 2016, pp. 687–697.

[21] Russell M. Cummings, S. A. M., "Overview of the DoD HPCMP Hypersonic Vehicle Simulation Initiative," *22nd AIAA International Space Planes and Hypersonics Systems and Technologies Conference*, , No. 2018-5205, 2018.

[22] L. Dale Thomas, J. L. R., Jeffrey M. Hanley, "NASA's Constellation Program: The Final Word," *Wiley Online Library*, 2012.

[23] Russell Daines, C. S., "Combined Rocket and Airbreathing Propulsion Systems for Space-Launch Applications," *Journal of Propulsion and Power*, Vol. 14, No. 5, 1998.

[24] Woolf, A. F., "Conventional Prompt Global Strike and Long-Range Ballistic Missiles: Background and Issues," *Congressional Research Service Report*, 2019.

[25] Mark T. Lewellyn, C. O. S., "Analysis at APL: A Historical Perspective," *John Hopkins APL Technical Digest*, Vol. 34, 2018, pp. 248–255.

[26] Gilmore, J. M., "2015 Assessment of the Ballistic Missile Defense System," , 2016.

[27] Behrens, A. J., "Joint Air and Missile Defense Mission Command: A Singular, Intelligent Multi-Domain Platform and Culture," , 2018.

[28] Mark R. Gruber, T. M., Mark A. HagenMaier, "Simulating inlet Distortion Effects in a Direct-Connect Scramjet Combustor," *42nd AIAA/ASME/SAE/ASEE Joint Propulsion Conference and Exhibit*, , No. 2006-4680, 2006.

[29] Brendan McGann, T. L., "Inlet Distortion Effects on Fuel Distribution and Ignition in Scramjet Cavity Flameholder," *Journal of Propulsion and Power*, Vol. 35, No. 3, 2019, pp. 601–613.

[30] Jimmy-John O.E. Hoste, R. J. G., Ian J. Taylor, "Numerical Modeling and Simulation of Supersonic Flows in Propulsion Systems by Open-Source Solvers," *21st AIAA International Space Planes and Hypersonics Technologies Conference*, , No. 2017-2411, 2017. doi:https://doi.org/10.2514/6.2017-2411.

[31] Anderson, J. D., *Hypersonic and High-Temperature Gas Dynamics, 2nd Edition*, AIAA, 2006.

[32] Anderson, J. D., *Fundamentals of Aerodynamics, 6th Edition*, McGraw Hill, 1221 Avenue of the Americas, New York, NY, 10020, 2017.

[33] Atcheson, B., "Schlieren-Based Flow Imaging," , 2004.

[34] H. Ockendon, S. A. E. G. F., J.R. Ockendon, "The Fanno Flow model for turbulent compressible flow," *Journal of Fluid Mechanics*, Vol. 445, 2001.

[35] Joseph A. Schetz, R. D. B., *Boundary Layer Analysis, Second Edition*, AIAA, 2011.

[36] Helen H. Lou, C. B. M., Daniel Chen, "Validation of a reduced combustion mechanism for light hydrocarbons," 2011.

[37] H. K. Narahari, V. K. J., H. S. Mukunda, "A Model of Combustion Monopropellants (AP) with Complex Gas Phase Kinetics," *Twentieth Symposium (International) on Combustion*, 1984.

[38] H. C. Hottel, A. H. B., G. C. Williams, "Application of Well-stirred Reactor Theory to the Prediction of Combustor Performance," *Combustion and Flame*, Vol. 2, 1958.

[39] Canstantin Rotaru, P. G. M., Mihai Andres-Mihaila, "An Extended Combustion Model for the Aircraft Turbojet Engine," *International Journal of Turbo and Jet Engines*, Vol. 31, 2013.

[40] Takeshi Kanda, F. O. Y. W., Goro Masuya, "Effect of Film Cooling/Regenerative Cooling on Scramjet Engine Performance," *Journal of Propulsion and Power*, Vol. 10, No. 5, 1994. doi:10.2514/3.23771.

[41] Tran, K., "One Dimensional Analysis Program for Scramjet and Ramjet Flowpaths," Master's thesis, Virginia Polytechnic Institute and State University, 2010.

[42] Cristian Birzer, C. J. D., "A Quasi-One-Dimensional Model of Hydrogen-Fuel Scramjet Combustors," *Journal of Propulsion and Power*, Vol. 25, 2009, pp. 1220–1225. doi: 10.2514/1.43716.

[43] Rodi, P. E., "Preliminary Ramjet/Scramjet Integration with Vehicles Using Osculating Flowfield Waverider Forebodies," *Applied Aerodynamics Conference*, Vol. 30, No. 2012-3223, 2012.

[44] A. Weiss, H. O., A. Grzona, "Behavior of Shock Trains in a Diverging duct," *Journal of Experiments in Fluids*, Vol. 49, 2009, pp. 355–365.

[45] "Cantera Documentation," , 2019. URL https://cantera.org/documentation/index.html.

[46] Chapra, S. C., *Applied Numerical Methods with MATLAB for Engineers and Scientists*, McGraw Hill, 1221 Avenue of the Americas, New York, NY, 10020, 2012.

[47] E. T. Curran, D. T. P., W. H. Heiser, "Fluid Phenomena in Scramjet Combustion Systems," *Annual review Fluid Mechanics*, 1996.

[48] M. R. Gruber, C. D. C., J. M. Donbar, "Mixing and Combustion Studies Using Cavity-Based Flameholders in Supersonic Flow," *Journal of Propulsion and Power*, Vol. 20, No. 5, 2004. doi:10.2514/1.5360.

[49] Hai Wang, A. L., "A Comprehensive Kinetic Model of Ethylene and Acetylene Oxidation at High Temperatures," Tech. rep., University of Delaware, 1998.

[50] Brian M. Adams, G. G., Michael S. Eldred, *Dakota, a Multilevel Parallel Object-Oriented Framework for Design Optimization Parameter Estimation, Uncertainty Quantification, and Sensitivity Analysis: Version 6.10 User's Manual*, 2019. URL https://dakota.sandia.gov/.

[51] Rassineux, A., "3D Mesh Adaption, Optimiztion of Tetrahedral Meshes by Advancing Front Technique," *Computer Methods in Applied Mechanics and Engineering*, 1996.

[52] Christophe Geuzaine, J.-F. R., "Gmsh Reference Manual," , 2019.

[53] Chris Long, N. S., *Heat Transfer*, BookBoon, 2009.

[54] Kaye, J., "Survey of Friction Coefficients, Recovery Factors, and Heat-Transfer Coefficients for Supersonic Flow," *Journal of the Aeronautical Sciences*, 1954, pp. 117–129. doi:10.2514/8.2940.

[55] Bertin, J. J., *Hypersonic Aerothermodynamics*, AIAA, 1994.

[56] C. A. Sleicher, M. W. R., "A Convenient for Heat Transfer to Constant and Variable Property Fluids in Turbulent Pipe Flow," *International Journal of Heat and Mass Transfer*, Vol. 18, 1975.

[57] Eckert, E. R. G., "Survey of Boundary layer Heat Transfer at High Velocities and High Temperatures," Tech. rep., Wright Air Development Center, 1960.

[58] Anderson, J. D., *Aircraft Performance and Design*, McGraw-Hill, 1221 Avenue of the Americas, New York, NY, 10020, 1999.

[59] Arora, J. S., *Introduction to Optimum Design, Fourth Edition*, Academic Press, 50 Hampshire Street, 5th Floor, Cambridge, MA, 02139, 2017.

[60] Brian M. Adams, K. R. D., William J. Bohnhoff, "Dakota Reference Manual," , 2019. URL https://dakota.sandia.gov/content/latest-reference-manual.